Eur. Phys. J. C (2010) 70: 635–657
DOI 10.1140/epjc/s10052-010-1480-6

THE EUROPEAN PHYSICAL JOURNAL C

Regular Article - Experimental Physics

Precise tests of low energy QCD from K_{e4} decay properties

The NA48/2 Collaboration

J.R. Batley[1], G. Kalmus[1], C. Lazzeroni[1,21], D.J. Munday[1], M.W. Slater[1,21], S.A. Wotton[1], R. Arcidiacono[19,2], G. Bocquet[2], N. Cabibbo[2,22], A. Ceccucci[2], D. Cundy[2,23], V. Falaleev[2], M. Fidecaro[2], L. Gatignon[2], A. Gonidec[2], W. Kubischta[2], A. Norton[2,6], A. Maier[2], M. Patel[2,24], A. Peters[2], S. Balev[2,3], P.L. Frabetti[3], E. Goudzovski[21,3], P. Hristov[2,3], V. Kekelidze[3], V. Kozhuharov[25,3], L. Litov[25,3], D. Madigozhin[3], E. Marinova[11,3], N. Molokanova[3], I. Polenkevich[3], Yu. Potrebenikov[3], S. Stoynev[10,3], A. Zinchenko[3], E. Monnier[26,4], E. Swallow[4], R. Winston[4], P. Rubin[27,5], A. Walker[5], W. Baldini[6], A. Cotta Ramusino[6], P. Dalpiaz[6], C. Damiani[6], M. Fiorini[2,6], A. Gianoli[6], M. Martini[6], F. Petrucci[6], M. Savrié[6], M. Scarpa[6], H. Wahl[6], A. Bizzeti[28,7], M. Lenti[7], M. Veltri[29,7], M. Calvetti[8], E. Celeghini[8], E. Iacopini[8], G. Ruggiero[14,8], M. Behler[9], K. Eppard[9], K. Kleinknecht[9], P. Marouelli[9], L. Masetti[9], U. Moosbrugger[9], C. Morales Morales[9], B. Renk[9], M. Wache[9], R. Wanke[9], A. Winhart[9], D. Coward[10,30], A. Dabrowski[10,2], T. Fonseca Martin[10,31], M. Shieh[10], M. Szleper[10], M. Velasco[10], M.D. Wood[10,32], P. Cenci[11], M. Pepe[11], M.C. Petrucci[11], G. Anzivino[12], E. Imbergamo[12], A. Nappi[12], M. Piccini[12], M. Raggi[12,33], M. Valdata-Nappi[12], C. Cerri[13], R. Fantechi[13], G. Collazuol[14], L. DiLella[14], G. Lamanna[14,2], I. Mannelli[14], A. Michetti[14], F. Costantini[15], N. Doble[15], L. Fiorini[15,34], S. Giudici[15], G. Pierazzini[15], M. Sozzi[15], S. Venditti[15], B. Bloch-Devaux[16,35,a], C. Cheshkov[16,36], J.B. Chèze[16], M. De Beer[16], J. Derré[16], G. Marel[16], E. Mazzucato[16], B. Peyaud[16], B. Vallage[16], M. Holder[17], M. Ziolkowski[17], C. Biino[18], N. Cartiglia[18], F. Marchetto[18], S. Bifani[19,37], M. Clemencic[19,2], S. Goy Lopez[19,38], H. Dibon[20], M. Jeitler[20], M. Markytan[20], I. Mikulec[20], G. Neuhofer[20], L. Widhalm[20]

[1] Cavendish Laboratory, University of Cambridge, Cambridge, CB3 0HE, UK[b]
[2] CERN, 1211 Genève 23, Switzerland
[3] Joint Institute for Nuclear Research, 141980 Dubna, Russian Federation
[4] The Enrico Fermi Institute, The University of Chicago, Chicago, IL 60126, USA
[5] Department of Physics and Astronomy, University of Edinburgh, JCMB King's Buildings, Edinburgh, EH9 3JZ, UK
[6] Dipartimento di Fisica dell'Università e Sezione dell'INFN di Ferrara, 44100 Ferrara, Italy
[7] Sezione dell'INFN di Firenze, 50125 Firenze, Italy
[8] Dipartimento di Fisica dell'Università e Sezione dell'INFN di Firenze, 50125 Firenze, Italy
[9] Institut für Physik, Universität Mainz, 55099 Mainz, Germany[c]
[10] Department of Physics and Astronomy, Northwestern University, Evanston, IL 60208-3112, USA
[11] Sezione dell'INFN di Perugia, 06100 Perugia, Italy
[12] Dipartimento di Fisica dell'Università e Sezione dell'INFN di Perugia, 06100 Perugia, Italy
[13] Sezione dell'INFN di Pisa, 56100 Pisa, Italy
[14] Scuola Normale Superiore e Sezione dell'INFN di Pisa, 56100 Pisa, Italy
[15] Dipartimento di Fisica dell'Università e Sezione dell'INFN di Pisa, 56100 Pisa, Italy
[16] DSM/IRFU - CEA Saclay, 91191, Gif-sur-Yvette, France
[17] Fachbereich Physik, Universität Siegen, 57068 Siegen, Germany[d]
[18] Sezione dell'INFN di Torino, 10125 Torino, Italy
[19] Dipartimento di Fisica Sperimentale dell'Università e Sezione dell'INFN di Torino, 10125 Torino, Italy
[20] Institut für Hochenergiephysik, Österreichische Akademie der Wissenschaften, 10560 Wien, Austria[e]
[21] University of Birmingham, Edgbaston, Birmingham, B15 2TT, UK
[22] Università di Roma "La Sapienza" e Sezzione dell'INFN di Roma, 00185 Roma, Italy
[23] Istituto di Cosmogeofisica del CNR di Torino, 10133 Torino, Italy
[24] Department of Physics, Imperial College, London, SW7 2BW, UK
[25] Faculty of Physics, University of Sofia "St. Kl. Ohridski", 1164 Sofia, Bulgaria
[26] Centre de Physique des Particules de Marseille, IN2P3-CNRS, Université de la Méditerranée, 13288 Marseille, France
[27] Department of Physics and Astronomy, George Mason University, Fairfax, VA 22030, USA
[28] Dipartimento di Fisica, Università di Modena e Reggio Emilia, 41100 Modena, Italy
[29] Istituto di Fisica, Università di Urbino, 61029 Urbino, Italy
[30] SLAC, Stanford University, Menlo Park, CA 94025, USA
[31] Laboratory for High Energy Physics, 3012 Bern, Switzerland
[32] UCLA, Los Angeles, CA 90024, USA
[33] Laboratori Nazionali di Frascati, 00044 Frascati (Rome), Italy

[34]Institut de Física d'Altes Energies, UAB, 08193 Bellaterra (Barcelona), Spain
[35]Dipartimento di Fisica Sperimentale dell'Università di Torino, 10125 Torino, Italy
[36]Institut de Physique Nucléaire de Lyon, IN2P3-CNRS, Université Lyon I, 69622 Villeurbanne, France
[37]University College Dublin School of Physics, Belfield, Dublin 4, Ireland
[38]Centro de Investigaciones Energeticas Medioambientales y Tecnologicas, 28040 Madrid, Spain

Received: 17 September 2010 / Published online: 6 November 2010

Abstract We report results from the analysis of the $K^{\pm} \to \pi^{+}\pi^{-}e^{\pm}\nu$ (K_{e4}) decay by the NA48/2 collaboration at the CERN SPS, based on the total statistics of 1.13 million decays collected in 2003–2004. The hadronic form factors in the S- and P-wave and their variation with energy are obtained. The phase difference between the S- and P-wave states of the $\pi\pi$ system is accurately measured and allows a precise determination of a_0^0 and a_0^2, the I = 0 and I = 2 S-wave $\pi\pi$ scattering lengths: $a_0^0 = 0.2220 \pm 0.0128_{\text{stat}} \pm 0.0050_{\text{syst}} \pm 0.0037_{\text{th}}$, $a_0^2 = -0.0432 \pm 0.0086_{\text{stat}} \pm 0.0034_{\text{syst}} \pm 0.0028_{\text{th}}$. Combination of this result with the other NA48/2 measurement obtained in the study of $K^{\pm} \to \pi^0\pi^0\pi^{\pm}$ decays brings an improved determination of a_0^0 and the first precise experimental measurement of a_0^2, providing a stringent test of Chiral Perturbation Theory predictions and lattice QCD calculations. Using constraints based on analyticity and chiral symmetry, even more precise values are obtained: $a_0^0 = 0.2196 \pm 0.0028_{\text{stat}} \pm 0.0020_{\text{syst}}$ and $a_0^2 = -0.0444 \pm 0.0007_{\text{stat}} \pm 0.0005_{\text{syst}} \pm 0.0008_{\text{ChPT}}$.

1 Introduction

At high energy, strong interactions between elementary particles are described by Quantum Chromo Dynamics (QCD) whose Lagrangian can be expanded in power series of the strong coupling constant. At low energy (below ∼1 GeV) the strong coupling becomes large and the perturbative description is no longer possible. Another approach, Chiral Perturbation Theory (ChPT), has been considered: it introduces an effective Lagrangian [1] where the elementary constituents are light pseudo-scalar mesons instead of quarks. The physical observables are then described by an expansion in terms of external momenta and light quark masses. At the cost of a number of free parameters (determined from experimental measurements), ChPT can quantitatively describe meson structure and form factors but can also compute hadronic contributions to some low energy observables like the $g-2$ of the muon which is very precisely measured [2, 3]. Testing the predictions of ChPT and its underlying assumptions is then of prime interest.

ChPT has been particularly powerful in describing $\pi\pi$ scattering at low energy and over the past 40 years, calculations at Leading Order (LO) and at the two subsequent Orders (NLO, NNLO) have converged toward very precise values of the underlying constants of the theory, the S-wave $\pi\pi$ scattering lengths in the isospin 0 and 2 states, denoted a_0^0 and a_0^2, respectively.

Experimental determinations of the scattering lengths have been pursued over more than four decades, but more recently, precise measurements have been obtained in several channels:

- The study of K_{e4} decays is of particular interest as it gives access to the final state interaction of two pions in absence of any other hadron. The asymmetry of the dilepton system with respect to the dipion system is related to the difference between the S- and P-wave $\pi\pi$ scattering phases for isospin states 0 and 1 ($\delta_0^0 - \delta_1^1$). Under the assumption of isospin symmetry, values of the scattering lengths a_0^0 and a_0^2 have been reported by NA48/2 [4] at the CERN SPS, based on a partial sample of 670 000 $K^{\pm}$ decays collected in 2003, E865 [5, 6] at the BNL AGS, based on 400 000 K^{+} decays and S118 [7] (often referred to as Geneva-Saclay Collaboration) at the CERN PS, based on 30 000 K^{+} decays. The results from the analysis of the full available statistics of NA48/2 (1.13 million decays) will be given here and discussed in detail.
- The study of $K^{\pm} \to \pi^0\pi^0\pi^{\pm}$ decays ($K_{3\pi}$) has shown evidence for a cusp-like structure in the $M_{\pi^0\pi^0}$ distribution, explained by re-scattering effects in the $\pi\pi$ system below and above the $2m_{\pi^{\pm}}$ threshold. This has been published by NA48/2 for partial (2.287×10^7 decays) [8] and total (6.031×10^7 decays) [9] statistics. The combination of the independent NA48/2 final results from the two channels, K_{e4} and $K_{3\pi}$ cusp, will be reported here and compared to the currently most precise theoretical predictions.

[a] e-mail: brigitte.bloch@cern.ch

[b]Funded by the UK Particle Physics and Astronomy Research Council.
[c]Funded by the German Federal Minister for Education and Research under contract 05HK1UM1/1.
[d]Funded by the German Federal Minister for Research and Technology (BMBF) under contract 056SI74.
[e]Funded by the Austrian Ministry for Traffic and Research under the contract GZ 616.360/2-IV GZ 616.363/2-VIII, and by the Fonds für Wissenschaft und Forschung FWF Nr. P08929-PHY.

– Another challenging approach is the formation of $\pi\pi$ atoms as studied by the DIRAC collaboration [10] at the CERN PS from 6 500 observed $\pi^+\pi^-$ pairs. The lifetime measurement of such pionium atoms is directly related to the underlying charge-exchange scattering process $\pi^+\pi^- \to \pi^0\pi^0$. The result of a larger sample analysis is also expected.

Isospin symmetry breaking effects have been fully considered in the last two processes which would not occur otherwise. With the achieved experimental precision from K_{e4} decays, mass effects ($m_{\pi^+} \neq m_{\pi^0}, m_u \neq m_d$), neglected in previous studies, should be included when relating phase measurements to scattering length values. The impact of these effects on the low energy QCD stringent tests performed will also be discussed.

2 Beam and detector

A sketch of the beam geometry and detector layout is shown in Fig. 1. The two simultaneous K^+ and K^- beams are produced by 400 GeVprimary protons from the CERN SPS impinging on a 40 cm long beryllium target. Opposite charge particles, with a central momentum of 60 GeV/c and a momentum band of ±3.8% (rms), are selected by two systems of dipole magnets (each forming an "achromat"), focusing quadrupoles, muon sweepers and collimators. At the entrance of the decay volume, a 114 m long evacuated vacuum tank, the beams contain ∼2.3×10^6 K^+ and ∼1.3×10^6 K^- per pulse of about 4.5 s duration with a flux ratio K^+/K^- close to 1.8. The two beams are focused ∼200 m downstream of the production target in front of the first spectrometer chamber [11]. The NA48 detector and its performances are described in full detail elsewhere [12]. The components used in the K_{e4} analysis are listed here:

– Charged particle momenta from $K^\pm$ decays are measured in a magnetic spectrometer consisting of four drift chambers (DCH1 through DCH4) and a large aperture dipole magnet located between the second and third chamber. Each chamber consists of four staggered double planes of sense wires along the horizontal, vertical and ±45° directions. The spectrometer is located in a tank filled with 95% purity helium at atmospheric pressure and separated from the decay volume by a thin (0.0031 radiation length thick) Kevlar® window to reduce multiple scattering. The spectrometer magnet gives a transverse momentum kick of 120 MeV/c to charged particles in the horizontal plane. The momentum resolution of the spectrometer is $\sigma(p)/p = (1.02 \oplus 0.044\ p)\%$ (p in GeV/c).
– A hodoscope (HOD) consisting of two planes of scintillators segmented into horizontal and vertical strips is used to trigger the detector readout on charged track topologies. The hodoscope surface is logically subdivided into 16 non-overlapping square regions. Its time resolution is ∼150 ps.
– A liquid-krypton calorimeter (LKr) measures the energy of electrons and photons. The transverse segmentation into 13248 2 cm × 2 cm projective cells and the 27 radiation length thickness result in an energy resolution $\sigma(E)/E = (3.2/\sqrt{E} \oplus 9.0/E \oplus 0.42)\%$ (E in GeV) and a space resolution for transverse position of isolated showers $\sigma_x = \sigma_y = (0.42/\sqrt{E} \oplus 0.06)$ cm. This allows to separate electrons ($E/p \sim 1$) from pions ($E/p < 1$).
– The muon veto counters (MUV) consist of one horizontal and one vertical plane of plastic scintillator slabs read out by photo-multipliers and preceded each by 0.8 m thick

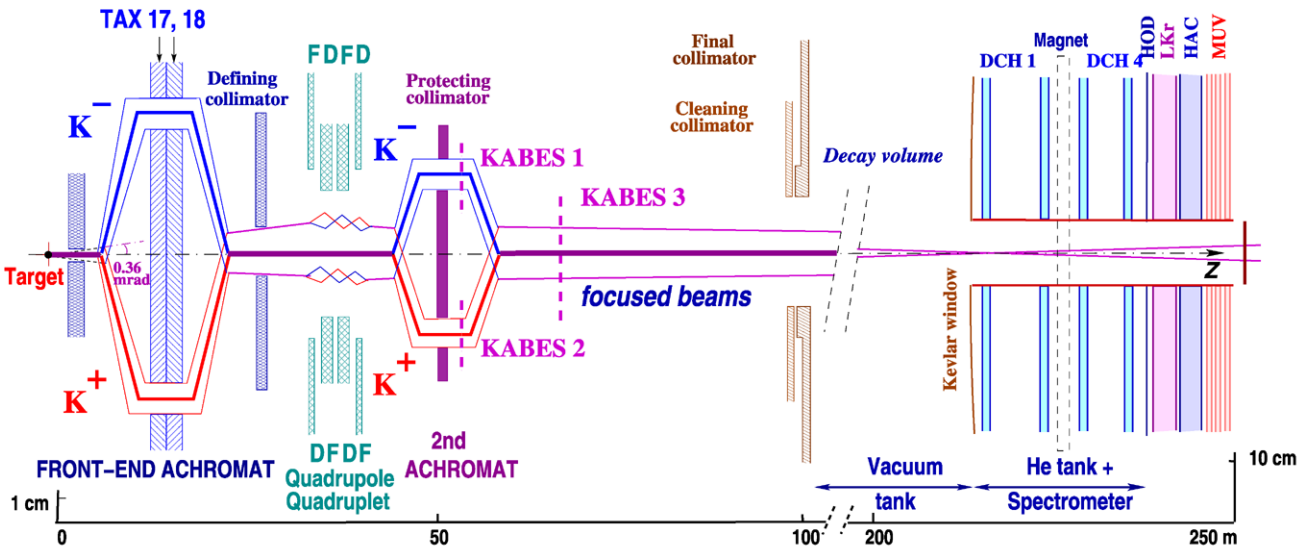

Fig. 1 Sketch of the NA48/2 beam line, decay volume and detectors. Note the different vertical scales in the left and right parts of the figure

iron absorbers. The MUV itself is also preceded by the hadron calorimeter (HAC, not used in this analysis) with a total thickness of 1.2 m of iron.
– A beam spectrometer (KABES), based on Micromegas amplification in a TPC [13], allows one to measure the incident kaon momentum with a relative precision better than 1%.
– A two-level trigger logic selects and flags events. At the first level (L1), charged track topologies are selected by requiring coincidences of hits in the two HOD planes in at least two of the 16 square regions. At the second level (L2), a farm of asynchronous microprocessors performs a fast reconstruction of tracks and runs a decision-taking algorithm. Three complementary configurations are used: (a) 2VTX, selecting events with at least three tracks forming consistent two-track vertices with the beam line; (b) 1VTX, selecting events with at least two tracks forming a vertex consistent with a beam particle decay; and (c) 1TRKP, which selects tracks originating from the beam line and kinematically inconsistent with $K^{\pm} \to \pi^{\pm}\pi^0$ decay. This trigger logic ensures a very high trigger efficiency for such topologies.

3 Event selection

Events from the whole data sample recorded in 2003 and 2004 were selected using criteria similar to those applied to the 2003 sample [4]. These criteria are recalled here for completeness, and complemented by the additional requirements applied in the final analysis.

3.1 Signal topology selection

The signal topology is characterized by three charged tracks consistent with a common decay vertex, with two opposite charge pions and one electron or positron. In addition, missing energy and transverse momentum should be allowed for the undetected neutrino.

In the 2004 run, the LKr calorimeter information was only recorded for a fraction of the 2VTX and 1VTX topologies, while events flagged as 1TRKP were fully recorded. An additional downscaling was applied off-line to the latter trigger configuration to ensure similar trigger conditions throughout the two years.

The whole data sample was then selected for three well reconstructed charged tracks. The timings of the three tracks, as measured from the DCH information, must agree within 6 ns, while the timings of the corresponding hodoscope signals must agree within 2 ns. The three-track reconstructed vertex position had to lie within a 5 cm radius transverse to the beam line and within 2 to 95 meters downstream of the final collimator. Two opposite sign pions ($E/p < 0.8$) and one electron or positron ($0.9 < E/p < 1.1$) were required. A minimum momentum requirement of 3 GeV/c (5 GeV/c) for the electron (pion) was applied while the maximum momentum sum was set at 70 GeV/c. The distance between any two tracks at DCH1 was required to be larger than 2 cm and the distance between any track and the beam line larger than 12 cm. The track impact at the LKr front face was required to fall within the active fiducial region and away from any dead cell by at least 2 cm to ensure reliable energy measurement. The track-to-track distance at the LKr front face had to be larger than 20 cm to prevent shower overlaps. No more than 3 GeV energy deposits in the calorimeter, not associated to tracks but in-time with the considered track combination, were allowed to eliminate events possibly biased by emission of hard photon(s). No track-associated signal in the MUV detector was allowed to reject possible $\pi \to \mu\nu$ decays in flight. The reconstructed three-track invariant mass (assigning the pion mass to each track) and the transverse momentum p_t relative to the beam axis had to be outside an ellipse centered on the kaon mass and zero p_t, with semi-axes 20 MeV/c^2 and 35 MeV/c, respectively, thus requiring a non-zero p_t value for the undetected neutrino and excluding $K^{\pm} \to \pi^+\pi^-\pi^{\pm}$ three-body decays.

The reconstruction of the kaon momentum under the assumption of a four-body decay with an undetected massless neutrino provides a more precise estimate than the 60 GeV/c average beam momentum. Imposing energy-momentum conservation in the decay and fixing the kaon mass and the beam direction to their nominal value, a quadratic equation in p_K, the kaon momentum, is obtained. If solutions exist in the range between 50 and 70 GeV/c, the event is kept and the solution closer to 60 GeV/c is assigned to p_K.

3.2 Background rejection

There are two main background sources: $K^{\pm} \to \pi^+\pi^-\pi^{\pm}$ decays with subsequent $\pi \to e\nu$ decay or a pion mis-identified as an electron; and $K^{\pm} \to \pi^{\pm}\pi^0(\pi^0)$ decays with subsequent Dalitz decay of a π^0 ($\pi^0_D \to e^+e^-\gamma$) with an electron mis-identified as a pion and photon(s) undetected. Additional selection criteria are applied against background events: the elliptic cut in the plane ($M_{3\pi}$, p_t) rejects $K^{\pm} \to \pi^+\pi^-\pi^{\pm}$ decays with one pion mis-identified as an electron but no missing mass in the $K_{3\pi}$ hypothesis and low p_t value. By varying the ellipse semi-axes one can change the amount of accepted contamination. Requiring the square invariant mass M_X^2 in the decay $K^{\pm} \to \pi^{\pm}X$ to be larger than 0.04 (GeV/c^2)^2 further rejects $K^{\pm} \to \pi^{\pm}\pi^0$ decays. An invariant mass of the e^+e^- system (assigning an electron mass to the opposite charge pion) larger than 0.03 GeV/c^2 ensures rejection of converted photons and of some multi-π^0 events. Additional rejection against pions mis-identified

as electrons is achieved by using a dedicated linear discriminant variable (LDA) based on shower properties (E/p, radial shower width and energy weighted track-cluster distance). The training of this variable has been performed on pion tracks from well reconstructed $K_{3\pi}$ events having $E/p > 0.9$, and electron tracks from K_{e3} ($K^{\pm} \to \pi^0 e^{\pm} \nu$) decays selected on the basis of kinematics only (missing mass of the ($K^{\pm} - \pi^0 - e^{\pm}$) system compatible with the neutrino mass). It provides a high, almost momentum independent, efficiency for electron tracks and additional rejection of pion tracks. The precise rejection level can be adjusted according to the discriminant variable value. To ensure a low level of contamination, the kaon momentum, reconstructed under the four-body assumption, was required to be within the range of 54 to 66 GeV/c. This momentum cut removes ∼40% of the remaining background along with a ∼2% loss of signal events (illustrated in Sect. 5).

The background contamination to signal "right sign" (RS) events ($\pi^+\pi^- e^{\pm}\nu$) is estimated from the observed "wrong sign" (WS) events ($\pi^{\pm}\pi^{\pm} e^{\pm}\nu$), which, assuming the validity of the $\Delta S = \Delta Q$ rule, can only be background. Such events are selected with the same criteria as the signal events apart from the requirement of two opposite sign pions which is changed to two same sign pions. The background contribution to RS signal events has the same magnitude as that measured from WS events if originating from $K^{\pm} \to \pi^+\pi^0(\pi^0)$ decays but has to be multiplied by a factor of 2 if originating from $K_{3\pi}$ decays because of the two equal charge pions. This factor has been cross-checked using Monte Carlo simulated events from the various background topologies.

A total of 1 130 703 K_{e4} candidates (726 367 K^+ and 404 336 K^-) were selected from a sample of $\sim 2.5 \times 10^{10}$ triggers recorded in 2003–2004. The subtracted background was estimated to $2 \times 3\,386$ ($2 \times 2\,109$ for K^+ and $2 \times 1\,277$ for K^-) events according to twice the observed numbers of WS events. The ∼0.6% relative background level was found to be constant throughout the two-year data taking.

4 Theoretical formulation

4.1 Kinematics

The decay $K^{\pm} \to \pi^+\pi^- e^{\pm}\nu$ is conveniently described using three different rest frames: the $K^{\pm}$ rest frame, the dipion rest frame and the dilepton rest frame. The kinematics is then fully described by the five Cabibbo–Maksymowicz variables [14, 15] as shown in the sketch of Fig. 2:

- $S_\pi = M_{\pi\pi}{}^2$, the square of the dipion invariant mass,
- $S_e = M_{e\nu}{}^2$, the square of the dilepton invariant mass,
- θ_π, the angle of the $\pi^{\pm}$ in the dipion rest frame with respect to the flight direction of the dipion in the $K^{\pm}$ rest frame,

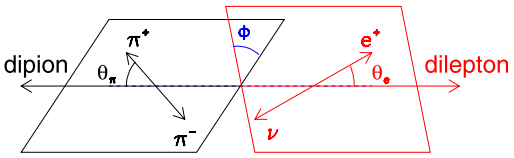

Fig. 2 Topology of the charged K^+_{e4} decay showing the angle definitions

- θ_e, the angle of the $e^{\pm}$ in the dilepton rest frame with respect to the flight direction of the dilepton in the $K^{\pm}$ rest frame,
- ϕ, the angle between the dipion and dilepton rest frames.

4.2 Decay probability

We recall the expression of the decay amplitude which is the product of the weak current of the leptonic part and the (V–A) current of the hadronic part:

$$\frac{G_w}{\sqrt{2}} V_{us}^* \bar{u}_\nu \gamma_\lambda (1-\gamma_5) v_e \, \langle \pi^+\pi^- | V^\lambda - A^\lambda | K^+ \rangle, \quad \text{where}$$

$$\langle \pi^+\pi^- | A^\lambda | K^+ \rangle = \frac{-i}{m_K} \big(F (\mathbf{p}_{\pi^+} + \mathbf{p}_{\pi^-})^\lambda + G (\mathbf{p}_{\pi^+} - \mathbf{p}_{\pi^-})^\lambda + R (\mathbf{p}_e + \mathbf{p}_\nu)^\lambda \big)$$

and

$$\langle \pi^+\pi^- | V^\lambda | K^+ \rangle = \frac{-H}{m_K^3} \epsilon^{\lambda\mu\rho\sigma} (\mathbf{p}_{\pi^+} + \mathbf{p}_{\pi^-} + \mathbf{p}_e + \mathbf{p}_\nu)_\mu \times (\mathbf{p}_{\pi^+} + \mathbf{p}_{\pi^-})_\rho (\mathbf{p}_{\pi^+} - \mathbf{p}_{\pi^-})_\sigma .$$

In the above expressions, $\mathbf{p}$ is the four-momentum of each particle, F, G, R are three axial-vector and H one vector complex form factors with the convention $\epsilon^{0123} = 1$.

The decay probability summed over lepton spins can be written as

$$d^5\Gamma = \frac{G_F^2 |V_{us}|^2}{2(4\pi)^6 m_K^5} \rho(S_\pi, S_e) I(S_\pi, S_e, \cos\theta_\pi, \cos\theta_e, \phi) \times dS_\pi \, dS_e \, d\cos\theta_\pi \, , \, d\cos\theta_e \, d\phi ,$$

where $\rho(S_\pi, S_e)$ is the phase space factor $X \sigma_\pi (1 - z_e)$, with $X = \frac{1}{2}\lambda^{1/2}(m_K^2, S_\pi, S_e)$, $\sigma_\pi = (1 - 4m_\pi^2/S_\pi)^{1/2}$, $z_e = \frac{m_e^2}{S_e}$, and $\lambda(a,b,c) = a^2 + b^2 + c^2 - 2(ab + ac + bc)$.

The function I, using four combinations of F, G, R, H complex hadronic form factors (F_i, $i = 1, 4$), reads [16–18]:

$$
\begin{aligned}
I = {} & 2(1-z_e)\big(I_1 + I_2\cos 2\theta_e + I_3\sin^2\theta_e\cdot\cos 2\phi \\
& + I_4\sin 2\theta_e\cdot\cos\phi + I_5\sin\theta_e\cdot\cos\phi \\
& + I_6\cos\theta_e + I_7\sin\theta_e\cdot\sin\phi \\
& + I_8\sin 2\theta_e\cdot\sin\phi + I_9\sin^2\theta_e\cdot\sin 2\phi\big),
\end{aligned}
$$

where

$$
\begin{aligned}
I_1 &= \frac{1}{4}\big((1+z_e)|F_1|^2 + \frac{1}{2}(3+z_e)\big(|F_2|^2+|F_3|^2\big)\sin^2\theta_\pi \\
&\quad + 2z_e|F_4|^2\big), \\
I_2 &= -\frac{1}{4}(1-z_e)\bigg(|F_1|^2 - \frac{1}{2}\big(|F_2|^2+|F_3|^2\big)\sin^2\theta_\pi\bigg), \\
I_3 &= -\frac{1}{4}(1-z_e)\big(|F_2|^2-|F_3|^2\big)\sin^2\theta_\pi, \\
I_4 &= \frac{1}{2}(1-z_e)\,\mathrm{Re}(F_1^*F_2)\sin\theta_\pi, \\
I_5 &= -\big(\mathrm{Re}(F_1^*F_3) + z_e\,\mathrm{Re}(F_4^*F_2)\big)\sin\theta_\pi, \\
I_6 &= -\big(\mathrm{Re}(F_2^*F_3)\sin^2\theta_\pi - z_e\,\mathrm{Re}(F_1^*F_4)\big), \\
I_7 &= -\big(\mathrm{Im}(F_1^*F_2) + z_e\,\mathrm{Im}(F_4^*F_3)\big)\sin\theta_\pi, \\
I_8 &= \frac{1}{2}(1-z_e)\,\mathrm{Im}(F_1^*F_3)\sin\theta_\pi, \\
I_9 &= -\frac{1}{2}(1-z_e)\,\mathrm{Im}(F_2^*F_3)\sin^2\theta_\pi.
\end{aligned}
$$

In K_{e4} decays, the electron mass can be neglected ($z_e = 0$) and the terms $(1 \pm z_e)$ become unity. One should also note that the form factor F_4 is always multiplied by z_e and thus does not contribute to the full expression.

With this simplification, the complex hadronic form factors F_i reduce to:

$$
\begin{aligned}
F_1 &= m_K^2(\gamma F + \alpha G\cos\theta_\pi), \\
F_2 &= m_K^2(\beta G), \qquad F_3 = m_K^2(\beta\gamma H),
\end{aligned}
$$

where one uses the three dimensionless complex form factors F, G (axial), H (vector), and three dimensionless combinations of the S_π and S_e invariants:

$$
\begin{aligned}
\alpha &= \sigma_\pi\big(m_K^2 - S_\pi - S_e\big)/2m_K^2, \\
\beta &= \sigma_\pi(S_\pi S_e)^{1/2}/m_K^2, \qquad \gamma = X/m_K^2,
\end{aligned}
$$

related by $\sigma_\pi\gamma = 2\sqrt{\alpha^2-\beta^2}$.

If T-invariance holds, the Watson theorem [19] tells us that a partial-wave amplitude of definite angular momentum l and isospin I must have the phase of the corresponding $\pi\pi$ amplitude δ_l^I.

Developing further F_1, F_2, F_3 in a partial wave expansion with respect to the variable $\cos\theta_\pi$ using Legendre functions $P_l(\cos\theta_\pi)$ and their derivative $P_l'(\cos\theta_\pi)$,

$$
\begin{aligned}
F_1/m_K^2 &= \sum_{l=0}^{\infty} P_l(\cos\theta_\pi)F_{1,l}e^{i\delta_l} \\
F_{2(3)}/m_K^2 &= \sum_{l=1}^{\infty} P_l'(\cos\theta_\pi)F_{2(3),l}e^{i\delta_l},
\end{aligned}
$$

one can now express the form factors F, G, H using explicitly the modulus and phase of each complex contribution. A D-wave contribution would appear as a $\cos^2\theta_\pi$ term for F and $\cos\theta_\pi$ terms for G, H with its own phase.

$$
\begin{aligned}
F &= F_s e^{i\delta_{fs}} + F_p e^{i\delta_{fp}}\cos\theta_\pi + F_d e^{i\delta_{fd}}\cos^2\theta_\pi, \\
G &= G_p e^{i\delta_{gp}} + G_d e^{i\delta_{gd}}\cos\theta_\pi, \\
H &= H_p e^{i\delta_{hp}} + H_d e^{i\delta_{hd}}\cos\theta_\pi.
\end{aligned} \tag{1}
$$

Limiting the expansion to S- and P-waves and considering a unique phase δ_p for all P-wave form factors in absence of CP violating weak phases, the function I is then expressed as the sum of 12 terms, each of them being the product of two factors, A_i, which depends only on the form factor magnitudes and one single phase δ ($= \delta_s - \delta_p$), and B_i which is function of the kinematical variables only (see Table 1):

$$
\begin{aligned}
I = {} & \sum_{i=1}^{12} A_i(F_s, F_p, G_p, H_p, \delta) \\
& \times B_i(S_\pi, S_e, \cos\theta_\pi, \cos\theta_e, \phi).
\end{aligned} \tag{2}
$$

Table 1 Contributions to the K_{e4} decay probability from S- and P-wave terms in absence of CP violating weak phases

Term	A_i	B_i
1	F_s^2	$\gamma^2\sin^2\theta_e$
2	F_p^2	$\gamma^2\cos^2\theta_\pi\sin^2\theta_e$
3	G_p^2	$\alpha^2\cos^2\theta_\pi\sin^2\theta_e$ $+ 2\alpha\beta\sin\theta_\pi\cos\theta_\pi\sin\theta_e\cos\theta_e\cos\phi$ $+ \beta^2\sin^2\theta_\pi(1-\sin^2\theta_e\cos^2\phi)$
4	H_p^2	$\beta^2\gamma^2\sin^2\theta_\pi(1-\sin^2\theta_e\sin^2\phi)$
5	$F_sF_p\cos\delta$	$2\gamma^2\cos\theta_\pi\sin^2\theta_e$
6	$F_sG_p\cos\delta$	$2\gamma\sin\theta_e(\beta\sin\theta_\pi\cos\theta_e\cos\phi$ $+ \alpha\cos\theta_\pi\sin\theta_e)$
7	$F_sG_p\sin\delta$	$2\beta\gamma\sin\theta_\pi\sin\theta_e\sin\phi$
8	$F_sH_p\cos\delta$	$-2\beta\gamma^2\sin\theta_\pi\sin\theta_e\cos\phi$
9	$F_sH_p\sin\delta$	$-2\beta\gamma^2\sin\theta_\pi\sin\theta_e\cos\theta_e\sin\phi$
10	F_pH_p	$-2\beta\gamma^2\sin\theta_\pi\cos\theta_\pi\sin\theta_e\cos\phi$
11	G_pH_p	$-2\beta\gamma\sin\theta_\pi(\beta\sin\theta_\pi\cos\theta_e$ $+ \alpha\cos\theta_\pi\sin\theta_e\cos\phi)$
12	F_pG_p	$2\gamma\cos\theta_\pi\sin\theta_e(\beta\sin\theta_\pi\cos\theta_e\cos\phi$ $+ \alpha\cos\theta_\pi\sin\theta_e)$

Going from K^+ to K^- under CPT conservation, θ_e should be replaced by $\pi - \theta_e$, ϕ should be replaced by $\pi + \phi$ and H_p by $-H_p$ [20]. Under the assumption of CP conservation, this is equivalent to obtaining the ϕ distribution of K^- decays from the ϕ distribution of K^+ decays with the same H_p value by changing ϕ to $-\phi$. This property can be verified in the expressions given in Table 1.

5 Monte Carlo simulation

Signal events were generated in the kaon rest frame according to the decay matrix element as given in Sect. 4.2 and with values of form factors as measured in [5–7], and then boosted to the laboratory frame. The incident kaon trajectory and momentum were generated taking into account the time variations of the beam properties for each kaon charge, and the decay vertex position according to the exponential decay law. As a precise description of the acceptance and resolution in the five-dimensional space of the kinematic variables is necessary, a detailed GEANT3-based [21] Monte Carlo (MC) simulation was used, including full detector geometry and material implementation, DCH alignment and local inefficiencies. A large time-weighted MC production was achieved, providing an event sample about 25 times larger than the data and reproducing the observed ratio $(K^+/K^-) = 1.8$. The same reconstruction and selection codes as for data were used, except for the timing cuts. The LDA cut was applied to the simulated electron candidates as a momentum-dependent efficiency. This represents the optimal implementation of the cut effect as it avoids reliance on the details of the shower developments, including fluctuations and limited statistics of the simulation. Two independent codes were used for the decay matrix element according to the Pais–Treiman formulation, one with a smooth phase shift variation [22] and constant form factors, the other with a more elaborated phase shift variation following ChPT prediction [23–25] and form factors depending on invariant masses (as published in [5, 6]). They were used in independent analyses of a subset of the data.

The quality of the simulation can be seen from the plots of Fig. 3 where distributions of simulated variables in the laboratory frame are compared to data distributions. Not only acceptance but also resolutions are well described in the simulation. Residual discrepancies will be studied in Sect. 7. Acceptances in the five-dimensional space are shown as two- and one-dimensional projections in Fig. 4 emphasizing their correlations. The experimental resolutions, projected on each of the five variables, vary smoothly across each spectrum. They are, respectively (the mean value corresponds to a mixture of $K^\pm$ in the same ratio as in the data):

rms	mean	variation across spectrum
$\sigma(M_{\pi\pi})$	1.5	increasing from 0.5 to 2.5 MeV/c^2,
$\sigma(M_{e\nu})$	9.6	decreasing from 13 to 6 MeV/c^2,
$\sigma(\cos\theta_\pi)$	0.052	decreasing from 0.058 ($\cos\theta_\pi = 0$) to 0.040 ($\cos\theta_\pi = \pm 1$),
$\sigma(\cos\theta_e)$	0.052	increasing from 0.025 ($\cos\theta_e = -1$) to 0.070 ($\cos\theta_e = 1$),
$\sigma(\phi)$	307	decreasing from 370 mrad ($\phi = 0$) to 240 mrad ($\phi = \pm\pi$).

Radiative corrections were implemented in the simulation in two successive steps.

- First, virtual photon exchange between charged particles is described by the classical Coulomb attraction/repulsion between two opposite/same charge particles ($i, j = \pi^+, \pi^-, e^\pm$) and applied as a weight to the K_{e4} decay probability according to the Gamow function:

$$C(S_{ij}) = \prod_{i \neq j} \frac{\omega_{ij}}{e^{\omega_{ij}} - 1}$$

  with $\omega_{ij} = 2\pi\alpha Q_i Q_j/\beta_{ij}$, where α is the fine structure constant, $Q_i Q_j = -1$ for opposite charge particles ($+1$ for same charge particles) and β_{ij} is the relative velocity (in unit of c) expressed as $\beta_{ij} = \sqrt{1 - \frac{4m_i^2 m_j^2}{(S_{ij} - m_i^2 - m_j^2)^2}}$ using the invariant mass S_{ij} of the (ij) system. The largest effect comes from the attraction between the two pions at low relative velocity, which distorts the $M_{\pi\pi}$ spectrum near threshold. The electron (positron) being always relativistic, its relative velocity is very close to 1 and the corresponding weight is a constant.
- Second, real photons are generated by the program PHOTOS version 2.15 [26] interfaced to the simulation. Only 10% of the events have photons adding up to more than 1 GeV in the laboratory frame. Furthermore the event selection reduces the acceptance for events with energetic photons. For these events, the resulting effect is a bias of the measured $M_{e\nu}$ and θ_e variables as hard photon emission mostly affects the electron kinematics.

6 Analysis method

As an extension of the method proposed originally in [16], based on partially integrated distributions of the Cabibbo–Maksymovicz variables in an ideal detector, we have chosen to work in the five-dimensional space to take into account the precise knowledge of the experimental acceptance and resolution. The high statistics now available allows a defi-

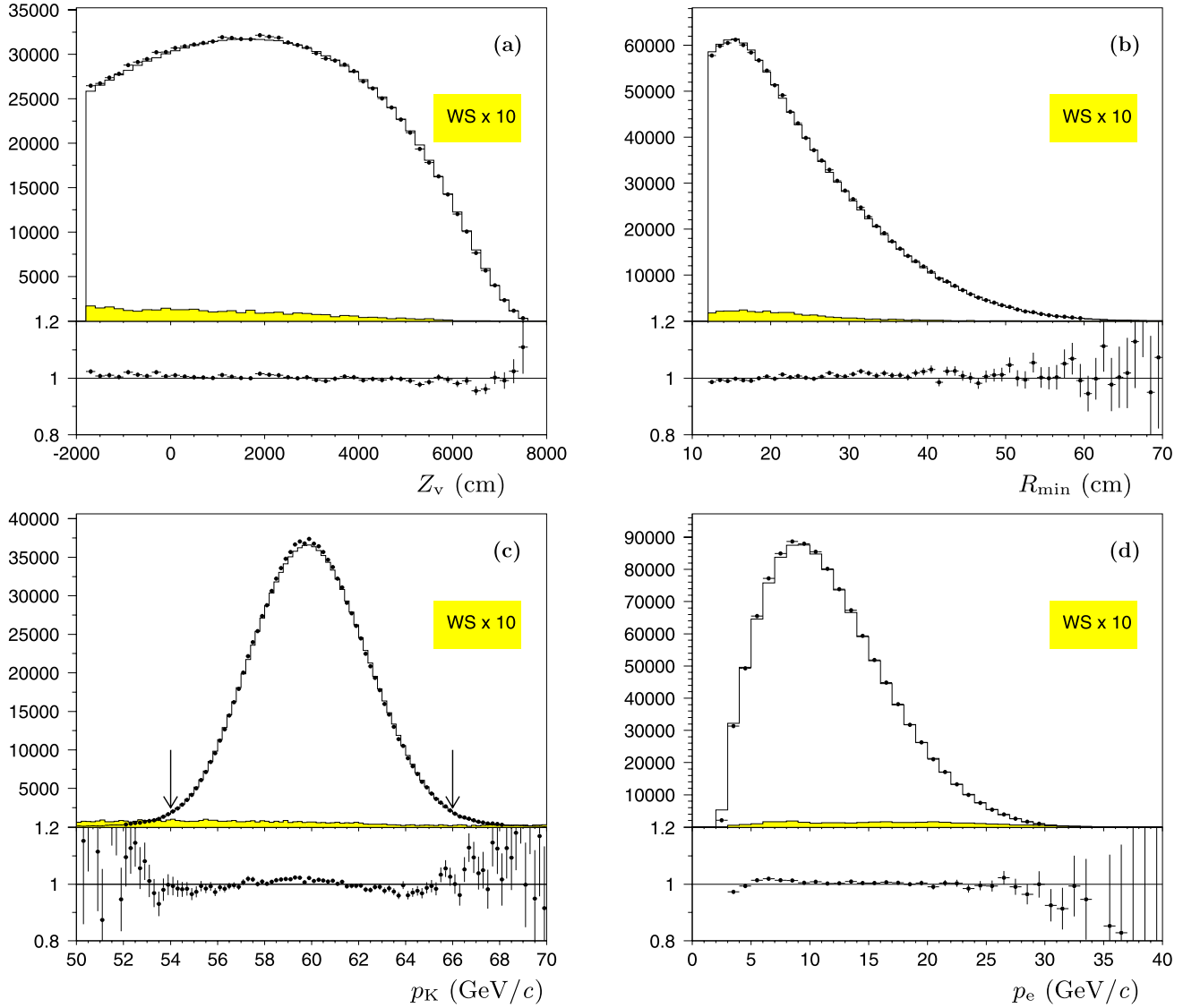

Fig. 3 Distributions of (**a**) the reconstructed vertex longitudinal position; (**b**) the minimum track radius at DCH1; (**c**) the reconstructed $K^{\pm}$ momentum; (**d**) the reconstructed electron momentum. Data (background subtracted) are shown as *full circles with error bars*, simulations as histograms and background (wrong sign events increased by a factor of 10 to be visible) as *shaded areas*. The *inserts* show the ratio of data to simulated distributions. The *arrows* on plot (**c**) show the reconstructed kaon momentum range selected in the final analysis. Errors shown are statistical only; residual discrepancies will be discussed in Sect. 7 (Systematic uncertainties)

nition of a grid of equal population boxes adapted to both detector acceptance and resolution, and to the form factor variations to be studied. There are of course many possible choices and we stick to the grid used in [4] for simplicity: the data sample is first distributed over ten $M_{\pi\pi}$ slices to follow the variation of physical parameters along this variable; each sub-sample is then distributed over five $M_{e\nu}$ equi-populated slices, then over five $\cos\theta_\pi$ slices, five $\cos\theta_e$ slices and 12 ϕ slices to ensure that correlations in the plane $(\cos\theta_e, \phi)$ are precisely described. This procedure results in a total of 15 000 five-dimensional boxes (N_{box}) of unequal sizes and achieves equal populations of 48 data events per box in the K^+ sample and 27 in the K^- sample, which are analyzed separately since the simultaneous $K^{\pm}$ beam geometries are not identical. A dedicated estimator (suited to account for Poisson fluctuations of the small number of events per box and limited simulation statistics) is used in the minimization procedure (as in previous analyses [4–7]). It is defined as

$$T^2 = 2\sum_{j=1}^{N_{box}} n_j \ln\left(\frac{n_j}{r_j}\left(1-\frac{1}{m_j+1}\right)\right) + (n_j+m_j+1)\ln\left(\frac{1+r_j/m_j}{1+n_j/(m_j+1)}\right),$$

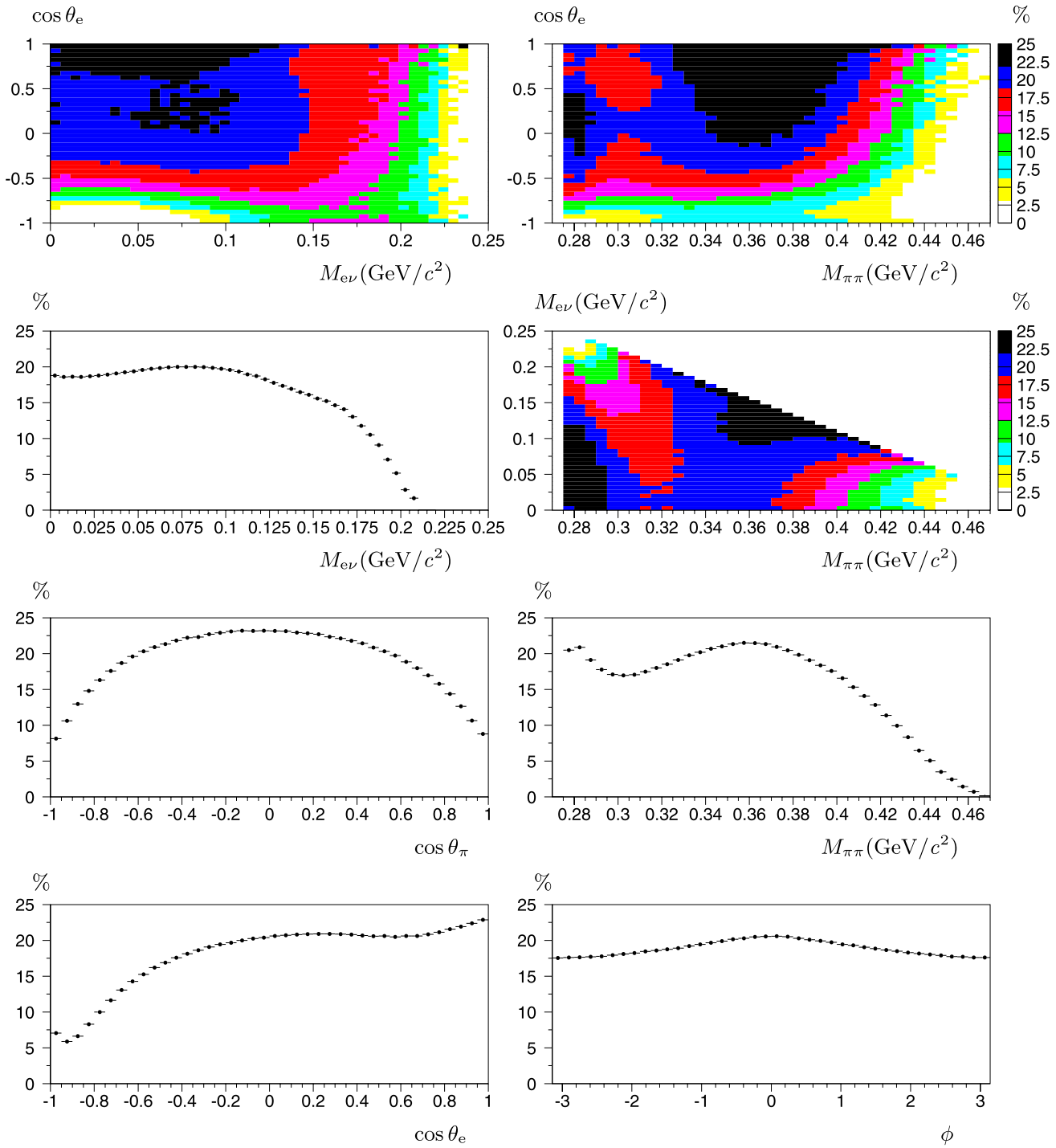

Fig. 4 Distribution of the acceptance (in %) as obtained from the simulation in the five-dimensional space and projected onto the $(M_{e\nu}, \cos\theta_e)$, $(M_{\pi\pi}, \cos\theta_e)$ and $(M_{\pi\pi}, M_{e\nu})$ planes and along the five kinematical variables. The smooth acceptance variation along single kinematical variables results from contributions of very different acceptance regions in the five-dimensional space

where n_j is the number of data events in box j, m_j is the number of observed simulated events in the same box and r_j is the number of expected simulated events ($r_j = m_j \cdot N_{\text{Data}}/N_{\text{MC}}^{\text{fit}} \cdot I(F,G,H,\delta)^{\text{fit}}/I(F,G,H,\delta)^{\text{gen}}$). The expression I is defined by (2) (Sect. 4.2) and computed for each event using the generated values of the kinematic variables and the current values of the fitted parameters $(F,G,H,\delta)^{\text{fit}}$, while $N_{\text{MC}}^{\text{fit}}$ is the corresponding total num-

ber of simulated events $\sum_{j=1}^{N_{\rm box}} m_j \cdot I(F,G,H,\delta)^{\rm fit}/I(F,G,H,\delta)^{\rm gen}$. This takes into account resolutions in the five-dimensional space and is independent of the particular set of form factors $(F,G,H,\delta)^{\rm gen}$ used at generation step provided that the simulated sample populated all regions of the five-dimensional space accessible to the data.

We note that the more "classical" Log-likelihood L and least squares χ^2 estimators

$$L = \sum_{j=1}^{N_{\rm box}} 2n_j \ln(n_j/r_j) + 2(r_j - n_j)$$

for large values of m_j,

$$\chi^2 = \sum_{j=1}^{N_{\rm box}} \frac{(r_j - n_j)^2}{n_j} \frac{m_j}{m_j + n_j}$$

for large values of m_j and n_j,

are almost equivalent to T^2 within the available statistics.

In this analysis, the branching fraction is not measured, so only relative form factors are accessible: F_p/F_s, G_p/F_s, H_p/F_s and the phase shift δ. Neglecting a possible $M_{e\nu}$ dependence and without prior assumption on the shape of their variation with $M_{\pi\pi}$, the form factors and phase shift are measured in independent $M_{\pi\pi}$ bins. Fits are performed in the four-dimensional space, separately for the K^+ and K^- samples but using the same $M_{\pi\pi}$ bin definitions. The results are found consistent for both charge signs and then combined in each bin according to their statistical weight. Identical results are obtained by fitting simultaneously the two independent samples to a single set of form factors and phase in the same $M_{\pi\pi}$ bins. The relative normalizations $(N_{\rm Data}/N_{\rm MC}^{\rm fit})$ are proportional to F_s^2 and are rescaled to have a value equal to unity at the $\pi\pi$ threshold. Last, values of F_p/F_s, G_p/F_s, H_p/F_s are deconvoluted of the observed F_s variation in each bin and plotted against $q^2 = (S_\pi/4m_\pi^2) - 1$ to investigate a possible further dependence. Potential variations with $M_{e\nu}$ are then explored and quantified when found significant.

In a second stage of the analysis, the observed variations of the form factors and phase shift with $M_{\pi\pi}$ and $M_{e\nu}$ are used to determine other parameter values through specific models. Series expansions of the variables $q^2 = (S_\pi/4m_\pi^2) - 1$ and $S_e/4m_\pi^2$ will be used to quantify the form factor variations (Sect. 8.1). More elaborated models related to the physical parameters (a_0^0 and a_0^2) will be used when studying the phase variation (Sect. 8.2).

7 Systematic uncertainties

Two independent analyses were performed on a large fraction of the 2003 data sample. They were based on different event selection and reconstruction, different detector corrections and different binning and fitting procedures. Consistent results were obtained, ensuring the robustness of the analysis. The final analysis was performed on the full statistics recorded over two years and follows one of the two validated analyses.

The studies reported in [4] have been repeated and extended to the whole data sample. Several systematic errors were limited by the available statistics and are now reduced. With respect to the analysis described in [4], the additional cut on the reconstructed kaon momentum ensures a lower relative background contamination (WS/RS = 0.0030 instead of 0.0046) and helps decreasing the impact of background related systematics. For each investigated item, the analysis was repeated varying one condition at a time and a systematic uncertainty was quoted for each fitted parameter in each $M_{\pi\pi}$ bin. A particular attention was given to possible bin-to-bin correlations, which are indeed observed in some cases.

- Fitting procedure: the number of boxes used in the fitting procedure was varied within a factor of 2, keeping, however, the same definition for the $10 M_{\pi\pi}$ bins. This last number was also extended to 12 and 15 bins. The grid definition was also varied as well as the estimator minimized in the fit. No visible bias was observed.
- Trigger efficiency: two independent methods to measure the high (∼99.3%) trigger efficiency were used. The first one considers K_{e4} selected candidates satisfying the Level 1 trigger condition (downscaled by 100 and thus based on small statistics) and measures the efficiency from events which satisfy the Level 2 trigger. The second approach focuses on $K^\pm \to \pi^\pm \pi^0_D$ events satisfying the Level 1 trigger condition, kinematic cuts and loose particle identification. Assigning a pion mass to both $\pi^\pm$ and opposite charge electron tracks allows coverage of the full $M_{\pi\pi}$ range with sufficient statistics. Both methods have been used to apply the trigger efficiency to the simulation in the five-dimensional space. As the efficiency is practically uniform and very stable over the two years, the overall effect is almost negligible.
- MUV efficiency: imperfect modeling of the MUV response to pion punch-through has been studied with pion tracks from fully reconstructed decays ($K_{3\pi}$, $K_{\pi\pi^0_D}$) and quantified as a function of the pion momentum. An additional inefficiency per pion track of 0.5 to 1.5% has been introduced in the simulation resulting in an average inefficiency of 1.7% varying between 1.3 and 2.3% over the five-dimensional space. The observed change in the fit parameters has been quoted as systematic uncertainty.
- Acceptance, resolution and beam geometry: the analysis method does not rely on the detailed matrix element assumptions, provided that the whole phase space is covered. Particular care was taken in controlling the geomet-

rical acceptance and in following the time-dependence of the beam geometry. The cut values on the longitudinal vertex position were varied in steps of few meters. The cut value on the minimum track-beam axis distance at DCH1 was varied in steps of one cm. Both variables are sensitive to the acceptance, trigger composition and beam geometry. The maximum effect observed for each variable was quoted as systematic uncertainty. A reweighting of the kaon simulated spectrum was considered in order to reproduce the data distribution (Fig. 3c) and the difference observed in the result was quoted as systematic error. It accounts for residual imperfections in the beam geometry and detector resolution modeling. These three effects of similar size have been added in quadrature under the same label in Table 2.

– Background contamination: the analysis was repeated subtracting the WS events according to their five-dimensional distributions, and scaled by a factor one, two or three. The dependence of each fitted parameter with the WS events scale factor was measured in each $M_{\pi\pi}$ bin. The scale factor for the background subtraction was cross-checked using a detailed simulation of contributing processes and found to be 2.0 ± 0.3. The effect of the 0.3 uncertainty is propagated to each point according to the measured slopes and quoted as systematic uncertainty (labeled background level in Table 2). The effect is bin-to-bin correlated, as expected.

The background measured from wrong sign (WS) events is observed at low S_π values as expected from $K_{3\pi}$ decays where S_π cannot exceed $(M_K - M_\pi)^2$, and shows a component clustering at $S_e = m_\pi^2$ from $\pi \to e\nu$ decays (Fig. 5). Varying the semi-axes of the elliptic cut in the plane $(M_{3\pi}, p_t)$ accepts different fractions and shapes of the $K_{3\pi}$ background. Results were found to be stable with respect to this cut without bin-to-bin correlation. Residual effects were quoted as systematic uncertainty (labeled background shape in Table 2).

– Electron identification: the final rejection against pions mis-identified as electrons ($E/p > 0.9$) is achieved by a cut on an LDA variable. In the simulation, the cut effect is applied as a momentum dependent efficiency. The cut value was varied from 0.85 to 0.90 (nominal cut) and 0.95. The analysis was repeated in the three conditions and the residual variation quoted as a systematic uncertainty.
– Radiative corrections: no systematic uncertainty was assigned to the Coulomb correction as its formulation is well established. The PHOTOS photon emission was switched off in the simulation to evaluate its effect on the fitted parameters. One tenth of the full effect was quoted as theoretical uncertainty on the radiative corrections. This is based on detailed comparisons between the PHOTOS and KLOR codes available for the $K^\pm \to \pi^\pm e^\mp \nu$ mode [27], and on more recent evaluations for the K_{e4} mode [28]. As expected, the effect comes mostly from removing events with hard photon emission.
– Dependence on S_e: in the first stage of the analysis, the form factors were assumed to be independent of $M_{e\nu}$. The effect of this assumption was explored by analyzing again the data with a simulation reweighted for a linear dependence of F_s on $S_e/4m_\pi^2$ with a slope of 0.068, as measured. The observed deviation between the two analyses was quoted as systematic uncertainty.

Many checks were performed to test the stability of the results, splitting the data in statistically independent subsamples according to the kaon charge, achromat polarity, dipole magnet polarity, decay vertex longitudinal position, transverse impact position of the electron on the calorimeter front face and data taking time. Results were compared in each bin and found to be consistent within the statistical errors.

In addition, a different reconstruction of the Cabibbo–Maksymowicz variables, based on the information of the KABES detector to measure precisely the kaon momentum and incident direction, improves the resolutions by ∼50% for the $\cos\theta_\pi$, $\cos\theta_e$, ϕ variables. However, as this information was only available for 65.6% of the event sample, and also affected by different systematic uncertainties (such as a mis-tagging rate of few percent), this alternative analysis was only used as a cross-check of the standard procedure. The results were found to be in good agreement and the statistical errors on the fitted parameters were reduced by 5 to 10% with respect to the standard analysis of the same subsample, yet this was not enough of an improvement to compensate for the 20% increase from the reduced statistics.

8 Results and interpretation

The detailed numerical results obtained in the ten independent slices of $M_{\pi\pi}$ are given in the Appendix (Table 7 to Table 12). As explained in the previous section, the systematic uncertainties do have a bin-to-bin correlated component, albeit much smaller than the uncorrelated one. In the tables, only the diagonal term of the matrix is quoted. The agreement between data and simulation distributions can be seen in Fig. 5 where K^+ and K^- data are added and compared to the sum of the simulated distributions using the common set of fitted parameters.

8.1 S- and P-wave form factors

Under the assumption of isospin symmetry, the form factors can be developed in a series expansion of the dimensionless invariants $q^2 = (S_\pi/4m_\pi^2) - 1$ and $S_e/4m_\pi^2$ [29].

Table 2 Systematic uncertainties (in units of 10^{-4}) affecting each of the dimensionless fitted parameters. The background level and S_e dependence contributions are 100% bin-to-bin correlated. Form factor description follows (3), (4) in Sect. 8.1. Scattering lengths (expressed in units of $1/m_{\pi^+}$) are given for Models B and C according to (6), (7) in Sect. 8.2

Source	f'_s/f_s	f''_s/f_s	f'_e/f_s	f_p/f_s	g_p/f_s	g'_p/f_s	h_p/f_s
Fit procedure	4	3	16	4	13	18	11
Trigger efficiency	25	23	1	4	9	13	1
MUV efficiency	2	1	5	<1	3	12	1
Acceptance/resolution	5	9	7	5	15	22	23
Background shape	16	15	4	12	39	44	27
Electron identification	5	10	8	7	28	43	54
Radiative corrections	11	14	27	9	35	69	21
Background level	20	16	51	22	65	72	8
S_e dependence	26	52	42	24	44	45	26
Total systematic	46	64	74	37	101	129	75
Statistical error	70	70	60	30	100	170	150

Source	Fit parameters		Fit parameter
	a_0^0	a_0^2	a_0^0
	Model B		Model C
Fit procedure	9	6	4
Trigger efficiency	6	4	2
MUV efficiency	10	7	<1
Acceptance/resolution	20	13	7
Background shape	31	18	10
Electron identification	14	10	7
Radiative corrections	19	12	5
Background level	19	10	7
S_e dependence	13	7	5
Total systematic	50	34	18
Statistical error	128	86	49

Two slope and one curvature terms are sufficient to describe the F_s form factor variation within the available statistics (the overall scale factor f_s is to be determined from the branching fraction, not reported here):

$$F_s = f_s\left(1 + f'_s/f_s q^2 + f''_s/f_s q^4 + f'_e/f_s S_e/4m_\pi^2\right), \qquad (3)$$

while two terms (offset and slope) are enough to describe the G_p form factor:

$$G_p/f_s = g_p/f_s + g'_p/f_s q^2, \qquad (4)$$

and two constants to describe the F_p and H_p form factors. The χ^2 of the fit to F_s is 111.5 for 81 degrees of freedom and blows up to 230.1 for 82 degrees of freedom if the S_e dependence is set to zero. The numerical results for all terms are given in Table 3 and displayed in Fig. 6. It has been checked that potential D-wave contributions (see (1)) are indeed consistent with zero and do not affect the S- and P-wave measured values.

Table 3 Results of the form factor measurements. When relevant, the correlations between fitted parameters are given

f'_s/f_s	$= 0.152$	$\pm 0.007_{stat}$	$\pm 0.005_{syst}$
f''_s/f_s	$= -0.073$	$\pm 0.007_{stat}$	$\pm 0.006_{syst}$
f'_e/f_s	$= 0.068$	$\pm 0.006_{stat}$	$\pm 0.007_{syst}$
f_p/f_s	$= -0.048$	$\pm 0.003_{stat}$	$\pm 0.004_{syst}$
g_p/f_s	$= 0.868$	$\pm 0.010_{stat}$	$\pm 0.010_{syst}$
g'_p/f_s	$= 0.089$	$\pm 0.017_{stat}$	$\pm 0.013_{syst}$
h_p/f_s	$= -0.398$	$\pm 0.015_{stat}$	$\pm 0.008_{syst}$

	correlations			
	f''_s/f_s	f'_e/f_s		g_p/f_s
f'_s/f_s	−0.954	0.080	g'_p/f_s	−0.914
f''_s/f_s		0.019		

Low energy constants (LEC L_i) which are parameters of ChPT can also be extracted from combined fits of meson masses, decay constants and form factor measurements.

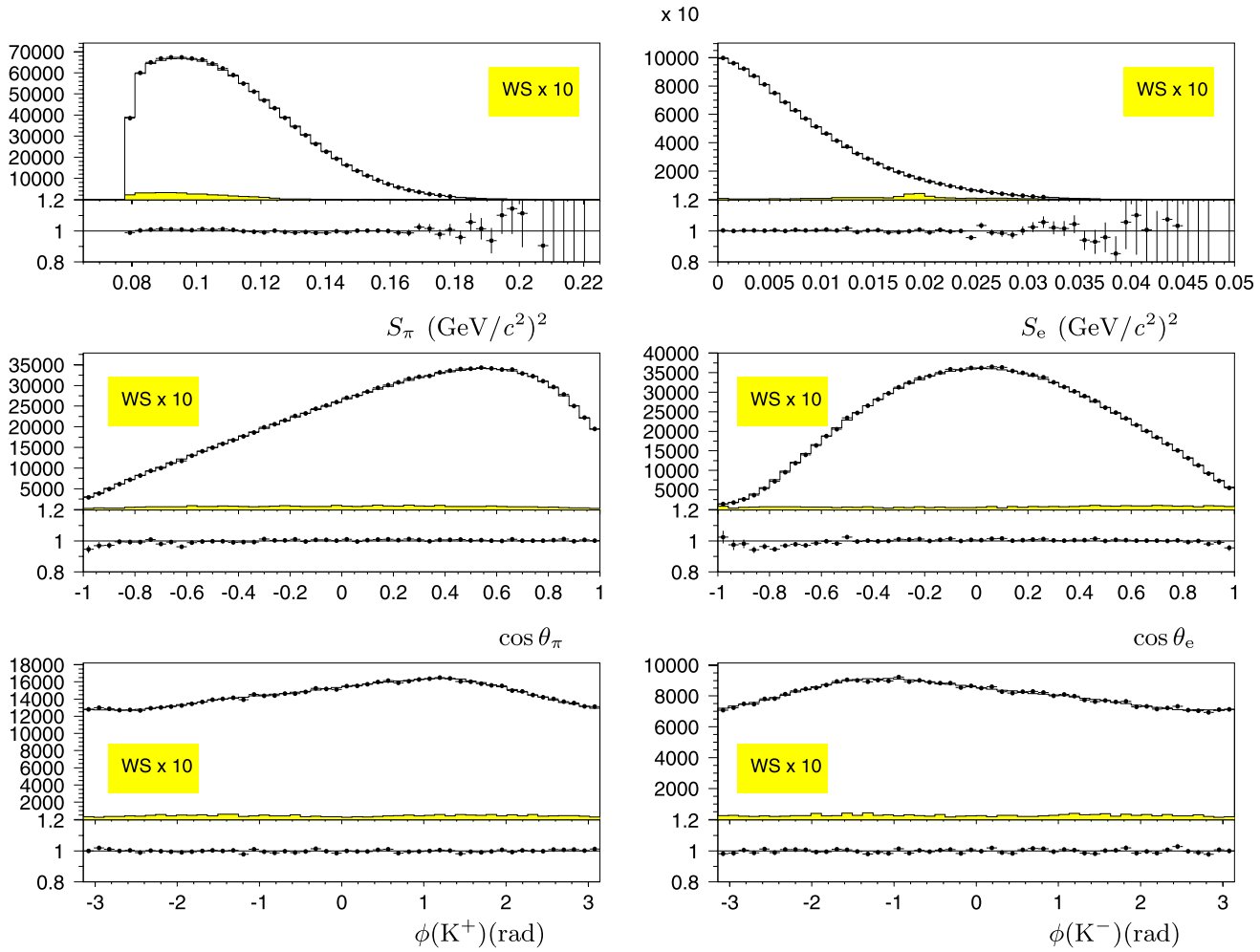

Fig. 5 Distribution of the Cabibbo–Maksymovicz variables projected from the five-dimensional space. The *full circles* are the $\mathrm{K}^\pm$ summed data after background subtraction, the histograms are the simulation with the best fit parameters, and the *shaded areas* correspond to the WS events multiplied by a factor of 10 to be visible. The *inserts* show the Data/Simulation ratios. The ϕ distributions are shown separately for K^+ and K^-. The errors shown are statistical only

This has been done in refs [18, 30–32] including successively S118, E865 and NA48/2 results [4] but such a study is beyond the scope of this article. It is not yet clear if the most recent NNLO calculations support the energy dependence of the now precisely measured form factors. Isospin breaking effects may have to be taken into account as suggested in some preliminary work [33, 34]. However, we can compare NA48/2 results with previous experimental results in terms of slopes and relative form factors using the absolute f_s value of each experiment as a normalization factor and propagating errors as uncorrelated in absence of any published correlation information. The available measurements are summarized in Table 4. While S118 results were limited by statistics and E865 errors were dominated by systematics, the NA48/2 values are now precise in both respects. The three sets of results are compatible within the experimental errors.

8.2 Phase shift and scattering lengths in the $\pi\pi$ system

8.2.1 Theoretical framework

To extract the $\pi\pi$ scattering lengths from the measurements of the phase shift $\delta = \delta_s - \delta_p$, more theoretical ingredients are needed. To perform a fair comparison of experimental results, we must take into account the evolution of the theoretical predictions over the last 30–40 years.

The Roy equations [35] were at the origin of many theoretical developments. These equations are based on the fundamental principles of analyticity, unitarity and crossing symmetries and allow a prediction of the $\pi\pi$ phase values close to threshold using experimental measurements above the matching point ($\sqrt{s} = 0.8$ GeV), and the subtraction constants a_0^0 and a_0^2, the isospin 0 and 2 S-wave scattering lengths (in units of $1/m_{\pi^+}$). One should note, however, that the two-pion system of the K_{e4} decay is never in the $\mathrm{I} = 2$

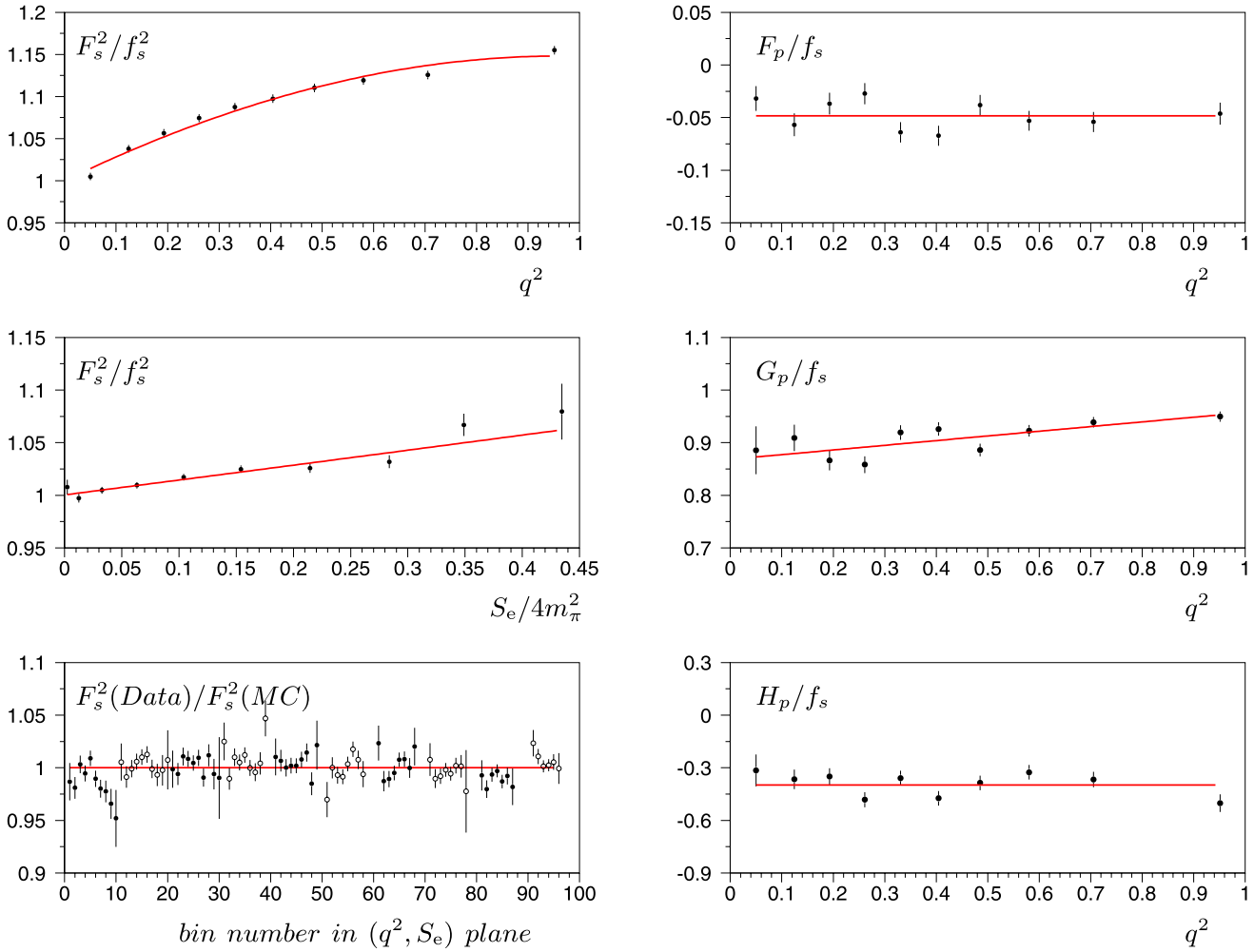

Fig. 6 Variation of the fitted form factors with q^2 and S_e. *Left column*: F_s^2 projected on to the q^2 axis assuming no S_e dependence and residual variation of the projection on the S_e axis when the q^2 dependence is accounted for. The *bottom plot* shows the ratio (Data/MC) after fit in each bin of the plane (q^2, S_e) displayed on a linear scale where S_e bins run in each q^2 bin. *Right column*: $F_p/f_s(\chi^2/\text{ndf} = 16.6/9)$, $G_p/f_s(\chi^2/\text{ndf} = 17.5/8)$ and $H_p/f_s(\chi^2/\text{ndf} = 18.2/9)$ versus q^2. The errors displayed in these figures are statistical only

state, but the combination $(2a_0^0 - 5a_0^2)$ enters as a subtraction constant and brings some sensitivity to a_0^2 when solving the Roy equations. Conversely, from measurements of the phases and using the Roy equations, one can determine the corresponding values of the subtraction constants.

We will consider three successive implementations of the solutions:

– *Model A*: in the mid 70's, several authors had given solutions of these equations [22, 36] and proposed a parametrization $\delta_0^0 = f(a_0^0, q^2)$. We will consider the parametrization of [22] which is explicitly given in [7] for $\delta = \delta_0^0 - \delta_1^1$ as

$$\sin 2\delta = 2\sigma_\pi \left(a_0^0 + bq^2\right), \tag{5}$$

where $b = b_0 - a_1^1$ is the difference between the S-wave slope with q^2 and the P-wave scattering length. In the plane (a_0^0, b) the two parameters are related by an empirical formula: $b = 0.19 - (a_0^0 - 0.15)^2$, where the slope b is a quadratic function of the S-wave scattering length within an uncertainty of ± 0.04 which reflects the input data precision. There is no dependence on a_0^2 in this formulation.

– *Model B*: numerical solutions of the Roy equations were published 25 years later by two groups [23, 37] with a parametrization of the phases δ_l^I with energy $(s = S_\pi)$:

$$\tan \delta_l^I(s) = \sigma_\pi q^{2l} \left\{A_l^I + B_l^I q^2 + C_l^I q^4 + D_l^I q^6\right\} \times \left(\frac{4m_\pi^2 - s_l^I}{s - s_l^I}\right), \tag{6}$$

where the Schenk coefficients $X_l^I (X = A, B, C, D, s)$ are written as a third degree polynomial expansion of the vari-

Table 4 Results of the form factor measurements for all K_{e4} experiments. The errors quoted in parentheses are statistical, then systematic (when available). Fits with one slope only and one slope and curvature for F_s have also been performed for direct comparison with previous experimental results. Due to lack of sensitivity, the values labeled by (∗) have been given by [5–7] only as a test. The value labeled by (†) is not exactly the same quantity as that measured by S118 and NA48/2

	S118 [7]	E865 [5, 6]	NA48/2
f_s	5.59(14)	5.75(2)(8)	n.a.
one term (q^2)			
f_s'/f_s	0.080(20)	0.079(15)	0.073(2)(2)
two terms (q^2, q^4)			
f_s'/f_s	–	0.184(17)(70)	0.147(7)(5)
f_s''/f_s	–	−0.104(21)(70)	−0.076(7)(6)
three terms ($q^2, q^4, S_e/4m_\pi^2$)			
f_s'/f_s	–	n.a.	0.152(7)(5)
f_s''/f_s	–	n.a.	−0.073(7)(6)
f_e'/f_s	–	$-0.056(18)(42)^*$	0.068(6)(7)
f_p/f_s	$0.009(32)^*$	$-0.059(17)(47)^\dagger$	−0.048(3)(4)
g_p/f_s	0.855(41)	0.809(9)(12)	0.868(10)(10)
g_p'/f_s	0.070(20)	0.120(19)(7)	0.089(17)(13)
h_p/f_s	−0.480(122)	−0.513(33)(35)	−0.398(15)(8)

ables $(a_0^0 - 0.225)$ and $(a_0^2 + 0.03706)$. Both predictions agree when using the same boundary conditions at the matching point $\sqrt{s} = 0.8$ GeV: $\delta_0^0 = 82.3°(\pm 3.4°)$ and $\delta_1^1 = 108.9°(\pm 2.0°)$.

The authors of ref. [37] have in addition parameterized the coefficients as a linear expansion around the values of the phases at the matching point.

In the plane (a_0^0, a_0^2), the values are constrained to lie within a band (called "Universal Band", UB) fixed by the input data above 0.8 GeV and the Roy equations, defined by the equation of the center line:

$$a_0^2 = -0.0849 + 0.232a_0^0 - 0.0865\left(a_0^0\right)^2$$

and by a width ± 0.0088.

– *Model C*: in the framework of ChPT, an additional constraint has been established [24, 25, 38] which can be used together with the Roy equations solutions discussed above to give more precise predictions lying within a ChPT band defined by the equation of the center line:

$$a_0^2 = -0.0444 + 0.236\left(a_0^0 - 0.220\right) - 0.61\left(a_0^0 - 0.220\right)^2 - 9.9\left(a_0^0 - 0.220\right)^3 \quad (7)$$

and by a reduced width ± 0.0008.

Including more phenomenological ingredients like the scalar radius of the pion, very precise predictions at NNLO have been made by the same authors:

$$a_0^0(\text{ChPT}) = 0.220 \pm 0.005_{\text{th}},$$
$$a_0^2(\text{ChPT}) = -0.0444 \pm 0.0010_{\text{th}}. \quad (8)$$

Because of the different formulations, a given set of phase measurements will translate to different values of the scattering lengths.

More recently, triggered by the early NA48/2 precise results [4], new theoretical work [39] has shown that isospin symmetry breaking may also alter the phases measured in K_{e4} decay when all mass effects ($m_{\pi^+} \neq m_{\pi^0}, m_u \neq m_d$), neglected so far in previous analyses, are considered. The measured phase of the I = 0 S-wave is no longer δ_0^0 but ψ_0^0:

$$\psi_0^0 = \frac{1}{32\pi F_\pi^2}\left((4\Delta_\pi + s)\sigma_\pm + \left(s - m_{\pi^0}^2\right)\left(1 + \frac{3}{2R}\right)\sigma_0\right) + \mathcal{O}\left(p^4\right), \quad (9)$$

where F_π is the pion decay constant, $s = S_\pi$,

$$\Delta_\pi = m_{\pi^\pm}^2 - m_{\pi^0}^2, \qquad R = \frac{m_s - \hat{m}}{m_d - m_u} \quad \text{and}$$
$$\sigma_x = \sqrt{1 - \frac{4m_{\pi^x}^2}{s}},$$

with $x = [\pm, 0]$.

Even if the difference between the mass-symmetric δ_0^0 ($\Delta_\pi = 0,\ 1/R = 0,\ \sigma_\pm = \sigma_0$) and ψ_0^0 is modest in terms of absolute magnitude (10 to 15 mrad) over the whole energy range accessible in K_{e4} decays, the coherent shift toward higher values of the phases has non-negligible implications when extracting scattering lengths from such measurements as shown in Fig. 7. These effects were of course present but neglected in the results of the S118 [7] and E865 [5, 6] experiments.

Other models, based on analyticity and unitarity but not using Roy equations have also been developed [40, 41]. They exploit the K_{e4} phase measurements associated or not with other $\pi\pi$ scattering results to extract a value for a_0^0 through a conformal transformation and an effective range function developed in a series of the variable $w(s) = \frac{\sqrt{s} - \sqrt{4m_K^2 - s}}{\sqrt{s} + \sqrt{4m_K^2 - s}}$ with coefficients $(B0, B1, \ldots)$. Results from such fits, using only the NA48/2 phase shift measurements will be reported as well.

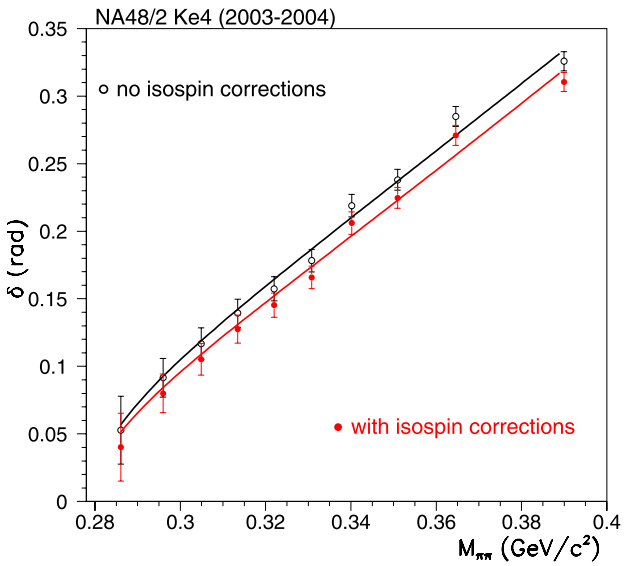

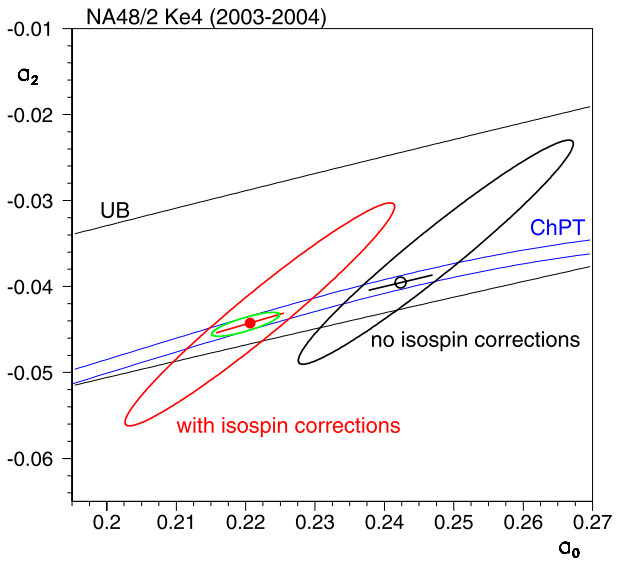

Fig. 7 (Color online) *Left*: Phase shift (δ) measurements without (*open circles*) and with (*full circles*) isospin mass effects correction from NA48/2 K_{e4} data. The *lines* correspond to the two-parameter fit within Model B. Errors are statistical only. *Right*: Fits of the NA48/2 K_{e4} data in the (a_0^0, a_0^2) plane without (*black*) and with (*red*) isospin mass effects. Errors are statistical only. *Ellipses* are 68% CL contours (Model B) and *circles* are the result of the one-parameter fit imposing the ChPT constraint (Model C). The *small* (*green*) *ellipse* corresponds to the best prediction from ChPT

8.2.2 NA48/2 results

We first focus on the most elaborated models B and C. The NA48/2 phase measurements are used as input to a two-parameter fit ((6), Model B) leading to:

$$a_0^0 = 0.2220 \pm 0.0128_{\text{stat}} \pm 0.0050_{\text{syst}} \pm 0.0037_{\text{th}},$$
$$a_0^2 = -0.0432 \pm 0.0086_{\text{stat}} \pm 0.0034_{\text{syst}} \pm 0.0028_{\text{th}},$$

with a 97% correlation coefficient and a χ^2 of 8.84 for 8 degrees of freedom for statistical errors only. The theoretical errors in the two-parameter fit have been estimated following the prescription described in [39] and are dominated by the experimental precision of the inputs to the Roy equation (for a_0^2) and the neglected higher order terms when introducing the mass effects (for a_0^0). The breakdown of the theoretical errors is given in Table 5. Using the additional ChPT constraint ((7), Model C), the one-parameter fit gives a χ^2/ndf of 8.85/9 for statistical errors only and the best fit value:

$$a_0^0 = 0.2206 \pm 0.0049_{\text{stat}} \pm 0.0018_{\text{syst}} \pm 0.0064_{\text{th}}$$

corresponding to ($a_0^2 = -0.0442$) from the ChPT constraint (see (7)). This result can be compared to the most precise prediction of ChPT (see (8)).

The result of a two-parameter fit based on analyticity only [40] from isospin corrected phase measurements leads to:

$$B0 = 10.229 \pm 2.433, \qquad B1 = -8.768 \pm 5.560,$$

Table 5 Contributions to the theoretical uncertainty on the scattering length values obtained in the two-parameter fit (see (6)) and the constrained fit (see (6) and (7)). The Bern solutions correspond to [23], the Orsay solutions to [37]

	Fit parameters		Fit parameter
	a_0^0	a_0^2	a_0^0
Roy equation solutions			
|(Bern) − (Orsay)|	0.0000	0.0006	0.0013
$\delta_0^0 \pm 3.4°$ at 0.8 GeV	0.0010	0.0027	0.0043
$\delta_1^1 \pm 2.0°$ at 0.8 GeV	0.0000	0.0002	0.0003
Isospin corrections			
$R = 37 \pm 5$	0.0005	0.0000	0.0008
$F_\pi = (86.2 \pm 0.5)$ MeV	0.0003	0.0001	0.0003
Higher orders	0.0035	0.0005	0.0042
Quadratic sum	0.0037	0.0028	0.0062
ChPT constraint width	–	–	0.0017
Quadratic sum	–	–	0.0064

with χ^2/ndf = 8.87/8 and 99.7% correlation, corresponding to $a_0^0 = 0.2255^{+0.0125}_{-0.0140\text{stat}}$, in agreement also with ChPT predictions for a_0^0, while no value can be given for a_0^2.

8.2.3 Discussion

We have repeated the S118 analysis within Model A (see (5)) using the published phase measurements and

found results consistent with the published scattering length value [7]. Then we have extended the analysis to Models B and C (see (6) and (7)) with and without the latest isospin mass effect corrections. The same exercise has been also performed using the E865 published phase values, after taking into account the recently published errata [42, 43] which solved most of the inconsistencies between the E865 global fit (which cannot be repeated by an external analysis) and the model independent fit (which can be repeated) results. Table 6 summarizes all fit results for existing K_{e4} data, as originally published, and also refitted under various conditions using the same model formulations.

A comparison of the two-parameter fit results of the three experiments under various model assumptions is shown in Fig. 8. The effect of the isospin corrections is marginal for S118 due to limited statistics but brings a significant shift for the E865 and NA48/2 results.

Figure 9-left shows all experimental phase measurements from K_{e4} data after correction for the isospin mass effects. Another interesting feature of Model C is the possibility to measure a_0^0 from each phase value by solving a polynomial expansion in q^2 along the ChPT constraint band [38]:

$$\delta = \frac{q}{\sqrt{1+q^2}}\left(a_0^0 + bq^2 + cq^4 + dq^6\right) \pm e, \quad \text{with}$$

$$b = 0.2527 + 0.151\left(a_0^0 - 0.22\right) + 1.14\left(a_0^0 - 0.22\right)^2 + 35.5\left(a_0^0 - 0.22\right)^3,$$

$$c = 0.0063 - 0.145\left(a_0^0 - 0.22\right), \qquad d = -0.0096 \quad \text{and}$$

$$e = 0.0035q^3 + 0.0015q^5.$$

Using such a method to extract a single value of a_0^0 implies that possible point-to-point correlations are negligible. This assumption is only approximately true, in particular because the systematic uncertainty from background subtraction and the isospin corrections are examples of point-to-point correlated effects. However, it is a meaningful check of the consistency of the experimental measurements within the model. Figure 9-right shows the values of a_0^0 obtained for

Table 6 Fits of experimental phase values within three models based on the Roy equations. In case of Model C, the value of a_0^2 is fixed by the constraint and given within parentheses

Model A (5)	Model B (6)	Model C (6), (7)
S118 [7] published Model A: $a_0^0 = 0.31 \pm 0.11$, $b = 0.11 \pm 0.16$		
no isospin correction		
$a_0^0 = 0.310 \pm 0.109$	$a_0^0 = 0.309 \pm 0.125$	$a_0^0 = 0.245 \pm 0.037$
$b = 0.110 \pm 0.190$	$a_0^2 = 0.013 \pm 0.105$	$(a_0^2 = -0.0390)$
including isospin correction (9)		
$a_0^0 = 0.282 \pm 0.110$	$a_0^0 = 0.280 \pm 0.124$	$a_0^0 = 0.224 \pm 0.040$
$b = 0.122 \pm 0.192$	$a_0^2 = 0.003 \pm 0.104$	$(a_0^2 = -0.0435)$
E865 [5, 6, 42, 43] published global fit results for two models:		
Model B: $a_0^0 = 0.203 \pm 0.033$, $a_0^2 = -0.055 \pm 0.023$		
Model C: $a_0^0 = 0.216 \pm 0.013$, $(a_0^2 = -0.0454 \pm 0.0031)$		
no isospin correction		
$a_0^0 = 0.213 \pm 0.035$	$a_0^0 = 0.206 \pm 0.033$	$a_0^0 = 0.235 \pm 0.013$
$b = 0.269 \pm 0.059$	$a_0^2 = -0.063 \pm 0.023$	$(a_0^2 = -0.0409)$
including isospin correction (9)		
$a_0^0 = 0.184 \pm 0.036$	$a_0^0 = 0.179 \pm 0.033$	$a_0^0 = 0.213 \pm 0.013$
$b = 0.284 \pm 0.060$	$a_0^2 = -0.072 \pm 0.023$	$(a_0^2 = -0.0461)$
NA48/2 final result		
no isospin correction		
$a_0^0 = 0.263 \pm 0.012$	$a_0^0 = 0.247 \pm 0.013$	$a_0^0 = 0.242 \pm 0.005$
$b = 0.191 \pm 0.018$	$a_0^2 = -0.036 \pm 0.009$	$(a_0^2 = -0.0395)$
including isospin correction (9)		
$a_0^0 = 0.236 \pm 0.013$	$a_0^0 = 0.222 \pm 0.013$	$a_0^0 = 0.221 \pm 0.005$
$b = 0.202 \pm 0.018$	$a_0^2 = -0.043 \pm 0.009$	$(a_0^2 = -0.0442)$

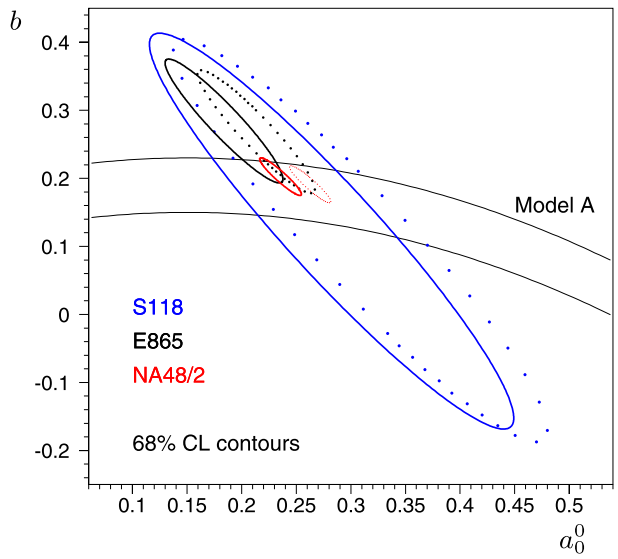

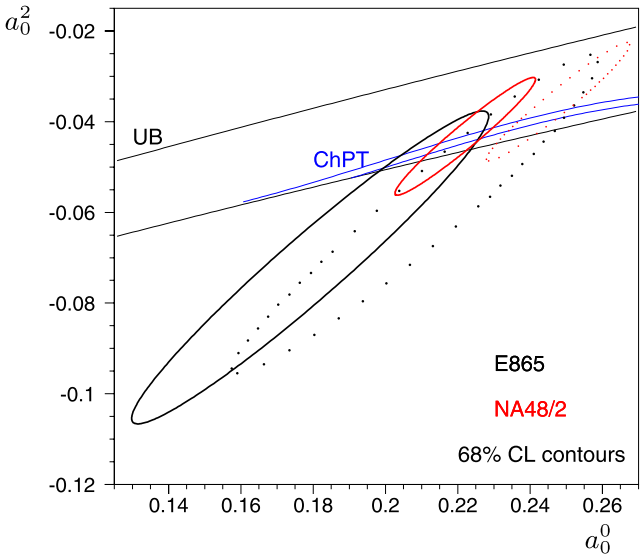

Fig. 8 *Left*: Results from all K_{e4} experiments in the (a_0^0, b) plane. The relation between the slope b and a_0^0 in Model A [22] is represented by the large band. Contours for two-parameter fits results at 68% CL are drawn as dotted before isospin corrections are applied and solid when applied. *Right*: Results from K_{e4} experiments in the (a_0^0, a_0^2) plane for Model B. The S118 experiment has little sensitivity to a_0^2 and is not shown here. The UB (Model B) and ChPT (Model C) bands show the region allowed by the Roy equation solutions and the additional ChPT constraint, respectively

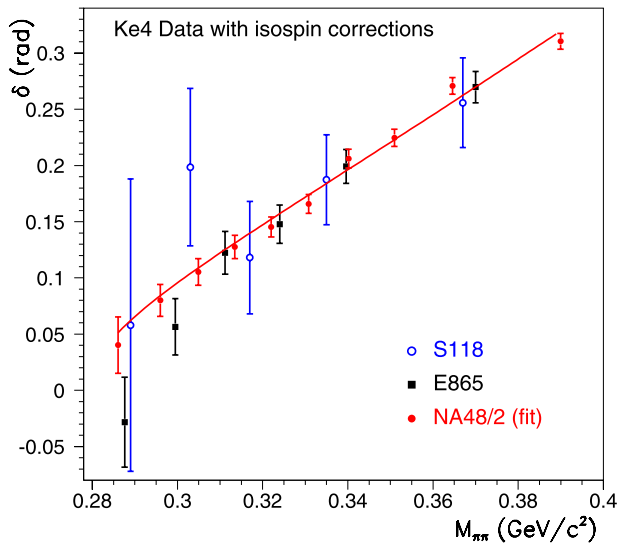

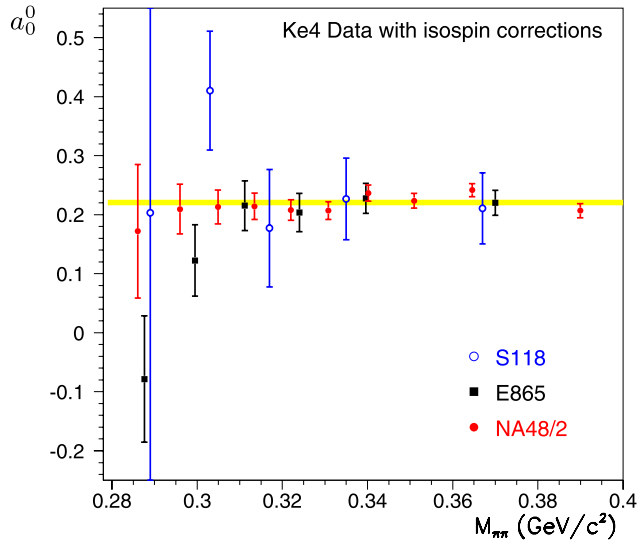

Fig. 9 *Left*: Phase shift (δ) measurements corrected for isospin mass effects for all K_{e4} available results. The *line* corresponds to the two-parameter fit of the NA48/2 data alone. *Right*: values obtained for each individual measurement from the inverted ChPT constraint. The *band* corresponds to the global fit over the NA48/2 data, including point to point correlations and is in agreement with the individual values. It means that the model gives a good description of the data points over the whole range

the 21 individual measurements of δ from the three experiments. The theoretical uncertainty e on the relation inverted in the fit has been added in quadrature to the statistical error to obtain the error on each point.

Going further in the framework of ChPT, the low energy constant (LEC) $\bar{l}_3$ can be extracted from the scattering length values determined from the NA48/2 phase measurements through the relations [38]:

$$a_0^0 = 0.225 - 1.6 \times 10^{-3}\bar{l}_3 - 1.3 \times 10^{-5}\bar{l}_3^2,$$

$$a_0^2 = -0.0434 - 3.6 \times 10^{-4}\bar{l}_3 - 4.3 \times 10^{-6}\bar{l}_3^2.$$

From the above equations, it should be noted that a_0^2 is five times less sensitive to $\bar{l}_3$ than a_0^0. From the most precise

value obtained within Model C, $a_0^0 = 0.2206 \pm 0.0049_{\text{stat}} \pm 0.0018_{\text{syst}}$, one can deduce a range for $\bar{l}_3$ between -0.55 and 5.75, in other words: $\bar{l}_3 = 2.6 \pm 3.2$ which is in very good agreement with the preferred value of ChPT [44] $\bar{l}_3 = 2.9 \pm 2.4$ and those obtained by lattice calculations [45] clustering around $\bar{l}_3 = 3 \pm 0.5$. The NA48/2 result excludes large negative values of $\bar{l}_3$ allowed in Generalized ChPT [37]. In this framework, it means that $\bar{l}_3$ brings only a few percent correction to the leading order term in the pion mass expression, product of the quark masses $(m_u + m_d)$ and the quark condensate $|\langle 0|\bar{u}u|0\rangle|$ in the chiral limit, normalized to the pion decay constant F_π [38]:

$$M_\pi^2 = M^2 - \frac{\bar{l}_3}{32\pi^2 F^2} M^4 + O\left(M^6\right)$$

$$\text{with } M^2 = (m_u + m_d)|\langle 0|\bar{u}u|0\rangle|/F_\pi^2.$$

8.3 Combination with other NA48/2 results

The analysis of the decay $K^\pm \to \pi^0\pi^0\pi^\pm$ by NA48/2 has enlightened another effect of the scattering lengths through the cusp observed in the $M_{\pi^0\pi^0}$ distribution as a consequence of re-scattering effects in the $\pi\pi$ system below and above the $2m_{\pi^\pm}$ threshold [8, 9].

The cusp and K_{e4} results are obviously statistically independent. They have systematic uncertainties of different origins (control of calorimetry and neutral trigger in one case, background and particle identification in the other) and show different correlations between the fitted scattering lengths (errors in parentheses are statistical then systematic):

	$K_{3\pi}$	K_{e4}
$a_0^0 =$		0.2220(128)(50)
$a_0^0 - a_0^2 =$	0.2571(48)(29)	
$a_0^2 =$	−0.0241(129)(96)	−0.0432(86)(34)
correlation	−0.839 (stat. only), −0.774 (all)	0.967 (stat. only), 0.969 (all)

The systematic errors quoted for the cusp results includes internal and external uncertainties, but no uncertainty associated to theory. In the K_{e4} result, the theoretical uncertainty contribution (Table 5) is even smaller than the experimental systematic error and thus has very little impact on the overall precision.

Neglecting potential (but small) common systematic contribution to the experimental errors, it is possible to combine the two measurements and to get a more precise result ($\chi^2/\text{ndf} = 1.84/2$):

$$a_0^0 = 0.2210 \pm 0.0047_{\text{stat}} \pm 0.0040_{\text{syst}},$$
$$a_0^2 = -0.0429 \pm 0.0044_{\text{stat}} \pm 0.0028_{\text{syst}},$$
$$a_0^0 - a_0^2 = 0.2639 \pm 0.0020_{\text{stat}} \pm 0.0015_{\text{syst}}.$$

The two input sets of values and their combination are displayed in Fig. 10. This last result, which does not require any additional theoretical ingredient, is in very good agreement with the most precise ChPT predictions (see (8)) given with a similar precision and recalled here:

$$a_0^0(\text{ChPT}) = 0.220 \pm 0.005_{\text{th}},$$
$$a_0^2(\text{ChPT}) = -0.0444 \pm 0.0010_{\text{th}},$$
$$a_0^0 - a_0^2(\text{ChPT}) = 0.264 \pm 0.004_{\text{th}}.$$

An alternative picture of the same results can be seen in Fig. 11a for the variables $a_0^0 - a_0^2$ and a_0^2 measured by NA48/2 and DIRAC experiments through three different processes.

It is worth comparing the now precise a_0^2 experimental measurement with very precise theoretical lattice QCD calculations involving also ChPT formulations:

$$a_0^2 = -0.04330 \pm 0.00042_{\text{stat} \oplus \text{syst}}$$

by the NPLQCD collaboration [46],

$$a_0^2 = -0.04385 \pm 0.00047_{\text{stat} \oplus \text{syst}}$$

by the ETM collaboration [47].

When using the ChPT constraint, the combined NA48/2 results become ($\chi^2/\text{ndf} = 1.87/1$):

$$a_0^0 = 0.2196 \pm 0.0028_{\text{stat}} \pm 0.0020_{\text{syst}},$$
$$a_0^0 - a_0^2 = 0.2640 \pm 0.0021_{\text{stat}} \pm 0.0015_{\text{syst}},$$
$$a_0^2 = -0.0444 \pm 0.0007_{\text{stat}} \pm 0.0005_{\text{syst}} \pm 0.0008_{\text{ChPT}},$$

where the last error on a_0^2 comes from the ChPT constraint uncertainty.

Such precise values of a_0^0 and a_0^2 can be used to evaluate the phase of ε', the direct CP violating amplitude in the process $K_L \to \pi\pi$ through interference between amplitudes in the isospin states 0 and 2. This phase is given by the value of $(\delta_0^2 - \delta_0^0 + \frac{\pi}{2})$ at the energy of the neutral kaon mass. Propagating the NA48/2 scattering length values and their correlated experimental errors to the phase values using the numerical solutions of Roy equations [23], we obtain $\delta_0^0 - \delta_0^2 = (47.67 \pm 0.06_{\text{exp}})$ degrees at M_{K^0} where the uncertainty corresponds to statistical and systematic errors added in quadrature. This result is fully consistent with the expectations of [23, 25] but with a much reduced experimental uncertainty. The width of the ChPT constraint translates to an additional uncertainty of ±0.3 degree to be added linearly to the experimental one. Using these values, we obtain the phase of ε', $\phi_{\varepsilon'} = (42.3 \pm 0.4)$ degrees.

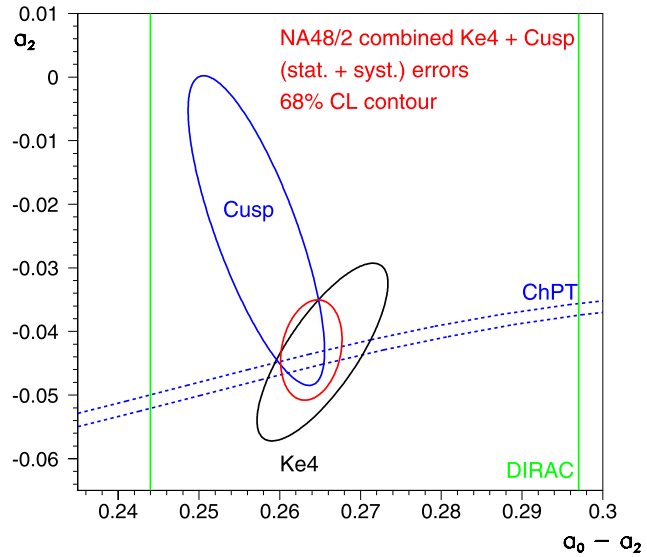

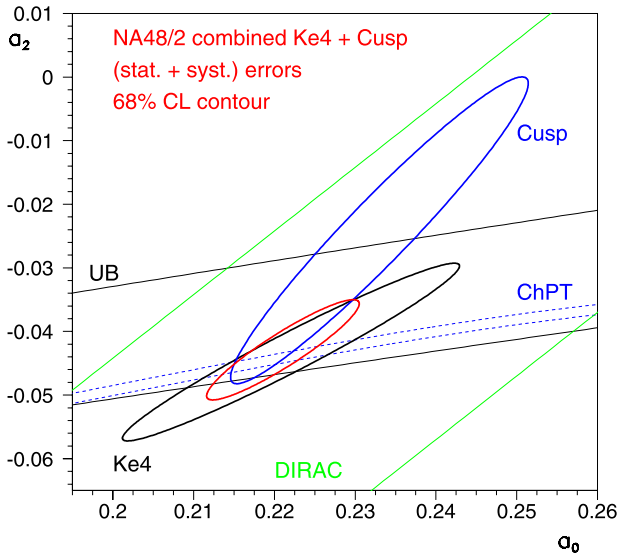

Fig. 10 (Color online) NA48/2 K_{e4} (*black*) and cusp (*blue*) results from the two-parameter fits in the $(a_0^0 - a_0^2, a_0^2)$ (*left*) and (a_0^0, a_0^2) (*right*) planes. In each plane the smallest (*red*) contour corresponds to the combination of the NA48/2 results. The correlation coefficient is then 0.21 in the left plane and 0.92 in the right plane. The *dashed lines* visualize the ChPT constraint band and the *solid* (*black*) lines the Universal Band. The other (*green*) lines correspond to the DIRAC result band [10]

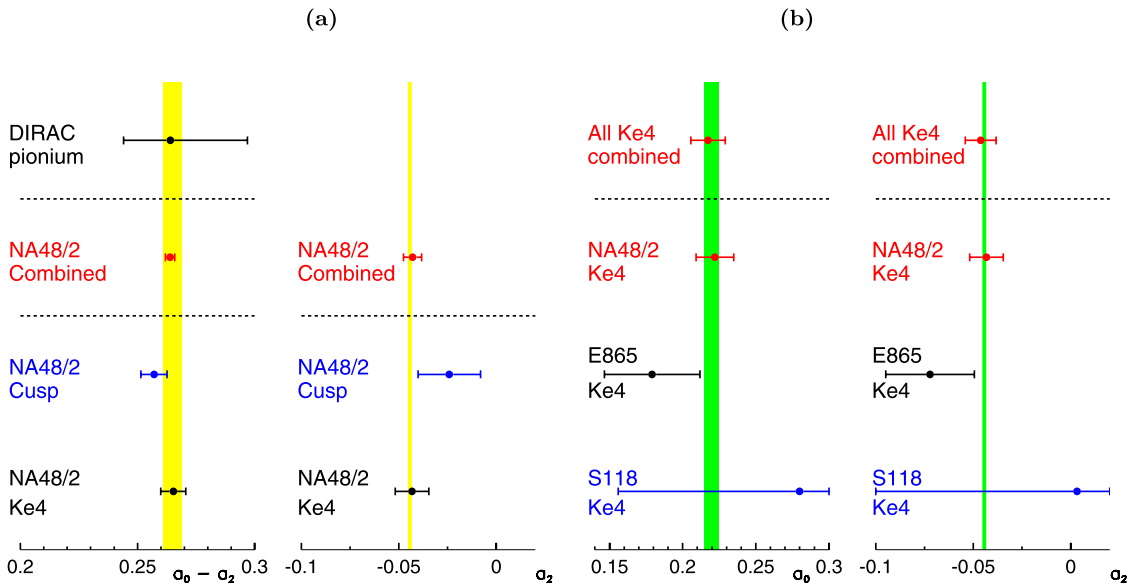

Fig. 11 (**a**): Two-parameter best fit values for $a_0^0 - a_0^2$ and a_0^2 from both NA48/2 channels and combined result. The DIRAC result is shown as well. (**b**): Two-parameter best fit values for a_0^0 and a_0^2 from each K_{e4} experiment and combined result (dominated by the NA48 precision). The right part of the large S118 error bar is truncated. Vertical bands correspond to the best predictions from ChPT: $a_0^0 = 0.220 \pm 0.005$, $a_0^0 - a_0^2 = 0.265 \pm 0.004$, $a_0^2 = -0.0444 \pm 0.0010$

9 Summary

9.1 NA48/2 results

From the study of 1.13 millions K_{e4} decays with both charge signs and with a low relative background of ∼0.6%, the S- and P-wave form factors and their variation with energy have been measured (Table 3). Evidence for a ∼5% contribution from F_p has been established; a constant H_p and linear G_p variation with S_π have been measured. The F_s form factor variation in the plane $(M_{\pi\pi}, M_{e\nu})$ can be described by a slope and curvature in S_π and a slope in S_e. The precise measurement of the phase shift of the $\pi\pi$ system has allowed to extract the scattering lengths a_0^0 and a_0^2 using the

Roy equations after correction for isospin breaking mass effects:

$$a_0^0 = 0.2220 \pm 0.0128_{\text{stat}} \pm 0.0050_{\text{syst}} \pm 0.0037_{\text{th}},$$
$$a_0^2 = -0.0432 \pm 0.0086_{\text{stat}} \pm 0.0034_{\text{syst}} \pm 0.0028_{\text{th}}.$$

This very sensitive test strongly confirms the predictions of Chiral Perturbation Theory and the underlying assumption of a large quark condensate contributing to the pion mass. Combining both NA48/2 K_{e4} and cusp results from independent analyses with different sensitivities, an even more precise set of values is obtained:

$$a_0^0 = 0.2210 \pm 0.0047_{\text{stat}} \pm 0.0040_{\text{syst}},$$
$$a_0^2 = -0.0429 \pm 0.0044_{\text{stat}} \pm 0.0028_{\text{syst}},$$
$$a_0^0 - a_0^2 = 0.2639 \pm 0.0020_{\text{stat}} \pm 0.0015_{\text{syst}}$$

which brings the first experimental determination of a_0^2 in perfect agreement with the currently very precise calculations of lattice QCD.

Using the additional constraint from ChPT (see (7)), the results from the K_{e4} analysis alone are:

$$a_0^0 = 0.2206 \pm 0.0049_{\text{stat}} \pm 0.0018_{\text{syst}} \pm 0.0064_{\text{th}},$$

and combined with the cusp results:

$$a_0^0 = 0.2196 \pm 0.0028_{\text{stat}} \pm 0.0020_{\text{syst}},$$
$$a_0^0 - a_0^2 = 0.2640 \pm 0.0021_{\text{stat}} \pm 0.0015_{\text{syst}},$$

corresponding to $a_0^2 = -0.0444 \pm 0.0007_{\text{stat}} \pm 0.0005_{\text{syst}} \pm 0.0008_{\text{ChPT}}$. These last values can be used to estimate the phase of the direct CP violating amplitude ε', giving $\phi_{\varepsilon'} = (42.3 \pm 0.4)$ degrees at the M_{K^0} energy.

9.2 Combination with other K_{e4} results

Combining K_{e4} NA48/2 results with previous experimental results [7, 42, 43] and applying isospin breaking corrections to all phase shift values, we obtain for the two-parameter fit ((6), Model B):

$$a_0^0 = 0.2173 \pm 0.0118_{\text{stat}} \pm 0.0043_{\text{syst}} \pm 0.0037_{\text{th}},$$
$$a_0^2 = -0.0462 \pm 0.0079_{\text{stat}} \pm 0.0030_{\text{syst}} \pm 0.0028_{\text{th}},$$

where all experimental errors are considered as independent between experiments and theoretical errors common to all experiments. Using the additional ChPT constraint ((7), Model C), we obtain

$$a_0^0 = 0.2198 \pm 0.0046_{\text{stat}} \pm 0.0016_{\text{syst}} \pm 0.0064_{\text{th}},$$

corresponding to

$$a_0^2 = -0.0445 \pm 0.0011_{\text{stat}} \pm 0.0004_{\text{syst}} \pm 0.0008_{\text{ChPT}}.$$

The new world average result is dominated by the NA48/2 experimental precision and illustrated in Fig. 11b.

Acknowledgements We gratefully acknowledge the CERN SPS accelerator and beam-line staff for the excellent performance of the beam and the technical staff of the participating institutes for their effort in the maintenance and operation of the detectors. We enjoyed constructive exchanges with S. Pislak and P. Truöl from the E865 collaboration and we also would like to thank all theory groups who expressed their interest in this work by fruitful discussions which triggered the latest developments of the analysis, in particular G. Colangelo, J. Gasser and the late J. Stern for their constant support and contribution.

Appendix: Fit results for independent $M_{\pi\pi}$ bins

The following tables give the definition of the $M_{\pi\pi}$ bins (Table 7) and the fit results for the four form factors (Table 8 to 11) and δ phase shift (Table 12) in each individual bin.

Table 7 Definition of the ten bins in $M_{\pi\pi}$: bin range, barycenter, event numbers ($K^+ + K^-$) and χ^2 of the fits for (2×1496) degrees of freedom in each bin

Bin number	$M_{\pi\pi}$ range (MeV/c^2)	$M_{\pi\pi}$ barycenter (MeV/c^2)
1	279.00–291.29	286.06
2	291.29–300.50	295.95
3	300.50–309.22	304.88
4	309.22–317.73	313.48
5	317.73–326.35	322.02
6	326.35–335.33	330.80
7	335.33–345.25	340.17
8	345.25–357.03	350.94
9	357.03–373.27	364.57
10	>373.27	389.95
Bin number	Number of events ($K^+ + K^-$)	χ^2 ndf = 2992
1	71940 + 39572	3087.66
2	72197 + 40354	2955.93
3	71671 + 40177	3092.96
4	71558 + 40164	2977.36
5	72725 + 40181	2954.31
6	72618 + 40290	2962.53
7	72817 + 39995	3010.69
8	73273 + 40751	3082.64
9	73232 + 41292	3113.97
10	74336 + 41560	2929.37

Table 8 Result of the fits for $F_s^2/F_s^2(0)$ (neglecting a possible M_{ev} dependence). An arbitrary scale has been applied to set $F_s^2/F_s^2(0) = 1$ at threshold. Values are given only as an indication of the variation as the analysis has been done in the plane (q^2, S_e). The quoted systematic errors correspond to the bin-to-bin uncorrelated part

Bin number	$F_s^2/F_s^2(0)$ value	Statistical error	Systematic error
1	1.0050	0.0030	0.0031
2	1.0379	0.0032	0.0016
3	1.0567	0.0032	0.0018
4	1.0743	0.0033	0.0018
5	1.0875	0.0033	0.0011
6	1.0975	0.0034	0.0016
7	1.1104	0.0034	0.0013
8	1.1191	0.0034	0.0010
9	1.1257	0.0034	0.0012
10	1.1550	0.0035	0.0060

Table 9 Result of the fits for $F_p/F_s(0)$. The quoted systematic errors correspond to the bin-to-bin uncorrelated part

Bin number	$F_p/F_s(0)$ value	Statistical error	Systematic error
1	−0.0318	0.0117	0.0027
2	−0.0569	0.0109	0.0060
3	−0.0367	0.0104	0.0057
4	−0.0273	0.0101	0.0056
5	−0.0641	0.0097	0.0072
6	−0.0672	0.0095	0.0066
7	−0.0381	0.0096	0.0080
8	−0.0530	0.0094	0.0057
9	−0.0542	0.0095	0.0055
10	−0.0462	0.0103	0.0057

Table 10 Result of the fits for $G_p/F_s(0)$. The quoted systematic errors correspond to the bin-to-bin uncorrelated part only

Bin number	$G_p/F_s(0)$ value	Statistical error	Systematic error
1	0.8856	0.0453	0.0116
2	0.9091	0.0249	0.0147
3	0.8661	0.0189	0.0104
4	0.8581	0.0160	0.0089
5	0.9193	0.0140	0.0102
6	0.9261	0.0128	0.0099
7	0.8859	0.0120	0.0103
8	0.9227	0.0109	0.0065
9	0.9389	0.0100	0.0052
10	0.9497	0.0096	0.0057

Table 11 Result of the fits for $H_p/F_s(0)$. The quoted systematic errors correspond to the bin-to-bin uncorrelated part only

Bin number	$H_p/F_s(0)$ value	Statistical error	Systematic error
1	−0.3147	0.0908	0.0339
2	−0.3659	0.0560	0.0135
3	−0.3498	0.0468	0.0171
4	−0.4820	0.0432	0.0126
5	−0.3585	0.0415	0.0171
6	−0.4741	0.0410	0.0154
7	−0.3861	0.0412	0.0273
8	−0.3253	0.0419	0.0193
9	−0.3673	0.0441	0.0380
10	−0.5022	0.0503	0.0310

Table 12 Result of the fits for the phase shift δ. The quoted systematic errors correspond to the bin-to-bin uncorrelated part only. The isospin correction (later subtracted) is given in the last column

Bin	δ value (mrad)	Statistical error (mrad)	Systematic error (mrad)	Isospin corr. (mrad)
1	52.775	25.102	7.934	12.542
2	91.564	14.267	7.787	11.555
3	116.819	11.772	4.743	11.543
4	139.295	10.399	3.908	11.760
5	157.357	8.927	2.327	12.071
6	178.237	8.354	1.723	12.441
7	218.901	8.329	4.821	12.866
8	238.024	7.714	2.261	13.377
9	284.913	7.425	2.168	14.044
10	325.778	7.011	1.769	15.322

References

1. S. Weinberg, Physica A **96**, 327 (1979)
2. G. Bennet et al., Phys. Rev. D **73**, 072003 (2006)
3. F.J.M. Farley, E. Picasso, Ann. Rev. Nucl. Part. Sci. **29**, 243 (1979)
4. J. Batley et al., Eur. Phys. J. C **54**, 411 (2008)
5. S. Pislak et al., Phys. Rev. Lett. **87**, 221801 (2001)
6. S. Pislak et al., Phys. Rev. D **67**, 072004 (2003)
7. L. Rosselet et al., Phys. Rev. D **15**, 574 (1977)
8. J. Batley et al., Phys. Lett. B **633**, 173 (2006)
9. J. Batley et al., Eur. Phys. J. C **64**, 589 (2009)
10. B. Adeva et al., Phys. Lett. B **619**, 50 (2005)
11. J. Batley et al., Eur. Phys. J. C **52**, 875 (2007)
12. V. Fanti et al., Nucl. Instrum. Methods A **574**, 433 (2007)
13. B. Peyaud, Nucl. Instrum. Methods A **535**, 247 (2004)
14. N. Cabibbo, A. Maksymowicz, Phys. Rev. B **137**, 438 (1965)
15. N. Cabibbo, A. Maksymowicz, Phys. Rev. **168**, 1926 (1968)
16. A. Pais, S. Treiman, Phys. Rev. **168**, 1858 (1968)
17. F. Berends, A. Donnachie, G. Oades, Phys. Rev. **171**, 1457 (1968)
18. J. Bijnens, G. Colangelo, J. Gasser, Nucl. Phys. B **427**, 427 (1994)
19. K.M. Watson, Phys. Rev. **88**, 1163 (1952)
20. T.D. Lee, C.S. Wu, Ann. Rev. Nucl. Sci. **16**, 471 (1966)

21. GEANT Description and Simulation Tool, CERN Program Library Long Writeup **W5013** (1994)
22. J.L. Basdevant, C.D. Froggatt, J.L. Petersen, Nucl. Phys. B **72**, 413 (1974)
23. B. Ananthanarayan, G. Colangelo, J. Gasser, H. Leutwyler, Phys. Rep. **353**, 207 (2001)
24. G. Colangelo, J. Gasser, H. Leutwyler, Phys. Lett. B **488**, 261 (2000)
25. G. Colangelo, J. Gasser, H. Leutwyler, Nucl. Phys. B **603**, 125 (2001)
26. E. Barberio, Z. Was (PHOTOS), Comput. Phys. Commun. **79**, 291 (1994)
27. A. Lai et al., Phys. Lett. B **645**, 26 (2007)
28. Q. Xu, Z. Was, Chin. Phys. C **34**, 889 (2010). arXiv:1001.0070 [hep-ph]
29. G. Amoros, J. Bijnens, J. Phys. G **25**, 1607 (1999)
30. G. Amoros, J. Bijnens, P. Talavera, Phys. Lett. B **480**, 71 (2000)
31. G. Amoros, J. Bijnens, P. Talavera, Nucl. Phys. B **602**, 87 (2001)
32. J. Bijnens, I. Jemos, PoS(CD09), 087 (2009)
33. A. Nehme, Phys. Rev. D **69**, 094012 (2004)
34. A. Nehme, Eur. Phys. J. C **40**, 367 (2005)
35. S. Roy, Phys. Lett. B **36**, 353 (1971)
36. C.D. Froggatt, J.L. Petersen, Nucl. Phys. B **129**, 89 (1977)
37. S. Descotes, N. Fuchs, L. Girlanda, J. Stern, Eur. Phys. J. C **24**, 469 (2002)
38. G. Colangelo, J. Gasser, H. Leutwyler, Phys. Rev. Lett. **86**, 5008 (2001)
39. G. Colangelo, J. Gasser, A. Rusetsky, Eur. Phys. J. C **59**, 777 (2009)
40. R. Garcia-Martin, J. Pelaez, F. Yndurain, Phys. Rev. D **76**, 074034 (2007)
41. R. Kaminski, J. Pelaez, F. Yndurain, Phys. Rev. D **77**, 054015 (2008)
42. S. Pislak et al., Phys. Rev. D **81**, 119903(E) (2010)
43. S. Pislak et al., Phys. Rev. Lett. **105**, 019901 (2010)
44. J. Gasser, H. Leutwyler, Ann. Phys. **158**, 142 (1984)
45. S. Aoki et al., Phys. Rev. D **79**, 034503 (2009) and references therein
46. S. Beane et al., Phys. Rev. D, **77**, 014505 (2008)
47. X. Feng, K. Jansen, D. Renner, Phys. Lett. B **684**, 268 (2010)